

VASPKIT: A User-friendly Interface Facilitating High-throughput Computing and Analysis Using VASP Code

Vei Wang

Department of Applied Physics, Xi'an University of Technology, Xi'an 710054, China

Nan Xu

College of Chemical and Biological Engineering, Zhejiang University, Hangzhou 310027, China

Jin-Cheng Liu

Department of Chemistry and Key Laboratory of Organic Optoelectronics & Molecular Engineering of Ministry of Education, Tsinghua University, Beijing 100084, China

Gang Tang

Theoretical Materials Physics, Q-MAT, CESAM, Université de Liège, Liège, Belgium

Wen-Tong Geng

School of Materials Science & Engineering, University of Science and Technology Beijing, Beijing 100083, China

Abstract

We present the VASPKIT, a Fortran 90 program that aims at providing a powerful and user-friendly interface to perform high throughput analysis of various material properties from the raw calculated data using the widely-used VASP code. It mainly includes the pre and post-processing modules. The former module is designed to prepare and manipulate input files such as the necessary input files generation, symmetry analysis, supercell transformation, band paths generation for a given crystal structure. The latter module is designed to extract and analyze the raw calculated data about elastic mechanics, electronic structure, charge/spin density, electrostatic potential, linear optical coefficients, wave function plots in real space, and etc. The program can be conveniently run under either the interactive user interface or command line mode. The command-line options allow to perform high-throughput calculations together with VASP code and bash scripts. This article gives an overview of the program structure and presents illustrative examples for some of its uses.

Keywords: High throughput; Elastic mechanics; Electronic structure; Optical; Molecular dynamics; Wave-function

PROGRAM SUMMARY

Program Title: VASPKIT

Licensing provisions: GPLv3

Programming language: Fortran 90

Computer: All computers with a Fortran compiler supporting at least Fortran 90.

Operating system: All operating systems with such a Fortran compiler.

External routines: Spglib [1], FFTPACK [2], libTetraBZ [3].

Nature of problem: This program has the purpose of providing a powerful and user-friendly interface to perform high-throughput calculations together with the widely-used VASP code.

Solution method: VASPKIT is able to extract, calculate and even plot the mechanical, electronic, optical and magnetic properties from density functional calculations together with bash and python scripts. It can run under either the interactive user interface or command line mode.

Restrictions: Only the VASP package is currently fully supported. It can be extended to work with files from other *ab-initio* packages.

Additional comments: This article describes version 1.2.0.

*E-mail address: wangvei@icloud.com

Running time: Problem dependent.

References

- [1] <https://atztogo.github.io/spglib/>
- [2] <https://www2.cisl.ucar.edu/resources/legacy/fft5>
- [3] <http://libtetraubz.osdn.jp/>

1. Introduction

Density functional theory (DFT) is one of the most popular methods to treat both model systems and realistic materials in a quantum mechanical way.[1, 2, 3, 4, 5] In condensed-matter physics, DFT is not only used to understand the observed behavior of solids, including the structural, mechanical, electronic, magnetic and optical properties of materials, but increasingly more to predict characteristics of compounds that have not yet been determined experimentally.[6, 7, 8, 9, 10, 11, 12] The last two decades have witnessed tremendous progress in the development of methods for first-principles calculations of materials properties and for simulations of processes in materials. There are dozens of electronic-structure packages have been developed based on DFT so far, such as Abinit[13], VASP[14, 15], Siesta[16], Quantum Espresso[17, 18], Elk[19] and WIEN2k[20], which are capable of exploring remarkable material properties. One of the common features for these packages is that the post-processing is required to plot or extract into a human-readable format from the raw calculated data. Several popular post-processing packages, such as Python Materials Genomics (pymatgen) [21] and Atomic Simulation Environment (ASE)[22], provide efficient and powerful interfaces to extract, plot and analyze the calculated raw data efficiently but require the users to be proficient in Python programming language.

In this article we will introduce a toolkit, here referred to as VASPKIT which is developed for providing a powerful and user-friendly input/output environment tool to perform initial setup for calculations and post-processing analysis to derive various material properties from the raw calculated data using VASP code. It is capable of calculating elastic, electronic, optical and catalytic properties including equation of state, elastic constants, effective mass of carriers, fermi surfaces, band structure unfolding for supercell models, linear optical coefficients, joint density of states, transition dipole moment, wave functions plots in real space, thermo energy correction, d -band center, and etc. In addition, it also provides the command line mode which allows to perform high-throughput calculations. For example, we recently performed high-throughput calculations to screen hundreds of two-dimensional (2D) semiconductors from near 1000 monolayers using this code together with VASP program and bash scripts.[23] The VASPKIT continues to be under development, with growing functionality, currently only supports VASP, however, it easy to extend it to working directly with files from other electronic structure packages. This program is written in Fortran 90 programming language and can run on UNIX, Linux, MacOS, and Microsoft Windows platforms.

The rest of this paper is organized as follows: In Section 2 we will briefly describes the workflow and basic features of the pre-processing module implemented in VASPKIT. Then in Section 3 we present the computational algorithms and some examples illustrating the capabilities of post-processing module in the VASPKIT code. Finally, our conclusions and outlook are presented in Section 4.

2. Pre-Processing Module

The workflow for the pre-processing module of VASPKIT package is illustrated in Fig. 1. First, the program reads POSCAR file and then prepares the rest three input files (INCAR, POTCAR and KPOINTS) to perform DFT calculations using VASP code. It also can edit structure file such as building supercell or generating the suggested band structure paths based on the algorithm proposed by Hinuma et al[24].

The crystal structures are often provided by basis vectors and point coordinates of labeled atoms. Lattice basis vectors \mathbf{A} are represented by three row vectors

$$\mathbf{A} = \begin{pmatrix} \mathbf{a} \\ \mathbf{b} \\ \mathbf{c} \end{pmatrix} = \begin{pmatrix} a_x & a_y & a_z \\ b_x & b_y & b_z \\ c_x & c_y & c_z \end{pmatrix}. \quad (1)$$

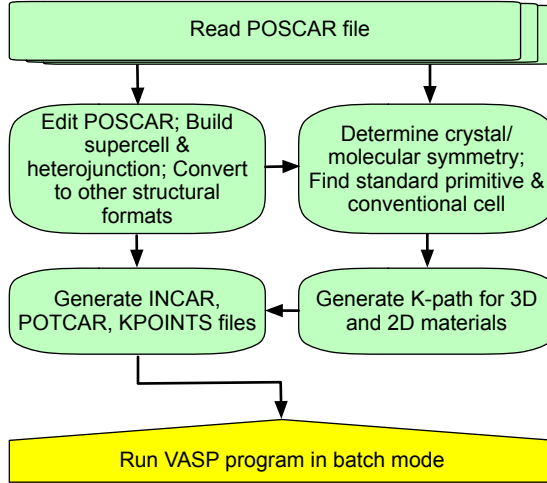


Figure 1: (Color online) Flow chart describing the workflow for the pre-processing module implemented into the VASPKIT package.

The position of a ion is represented by a row vector either in fractional coordinates (x, y, z) with respect to basis vector lengths or in Cartesian coordinates (X, Y, Z)

$$\begin{pmatrix} X \\ Y \\ Z \end{pmatrix} = \mathbf{A}^T \begin{pmatrix} x \\ y \\ z \end{pmatrix} = \begin{pmatrix} a_x & b_x & c_x \\ a_y & b_y & c_y \\ a_z & b_z & c_z \end{pmatrix} \begin{pmatrix} x \\ y \\ z \end{pmatrix}. \quad (2)$$

The convention from a choice of lattice basis vectors to another choice of basis vectors is related with transformation matrix M

$$\begin{pmatrix} \mathbf{a}' \\ \mathbf{b}' \\ \mathbf{c}' \end{pmatrix} = M \cdot \begin{pmatrix} \mathbf{a} \\ \mathbf{b} \\ \mathbf{c} \end{pmatrix}. \quad (3)$$

VASPKIT can determine the crystal symmetry information, or find the conventional/primitive cell for a given lattice by employing the symmetry analysis library Spglib[25]. Furthermore, it can also convert POSCAR file to several widely-used structural formats, such as XCrysDen (xsf) [26], Crystallographic Information Framework (CIF)[27] or Protein Data Bank (PDB) formats[28].

3. Post-Processing Module

Fig. 2 displays an overview of the post-processing features which have been implemented into the VASPKIT package. Next we will present the computational algorithms and some examples to illustrate the capabilities of the post-processing module.

3.1. Equations of State

Thermodynamic equations of state (EOS) for crystalline solids describe material behaviors under changes in pressure, volume, entropy and temperature. The workflow of EOS utility is similar to that of the elastic constant one as presented in Fig. 4. There are 12 EOS models have been implemented into the EOS utility. Furthermore, pressure and enthalpy as function of volume are also provided. Very recently, Latimer et al. evaluated the quality of fit for 8 widely used EOS models as summarized in Table 1 across 87 elements and over 100 compounds.[29] They found that the Birch-Euler, Tait, and Vinet equations give the best overall quality of fit to calculated energy-volume curves as compared to the other equations under examination. However, the inconsistent among these investigated equations is not significant. As a benchmark test, we present the PBE-calculated energy versus volume results for diamond using different EOS models as listed in Table 1. It it found that the agreement among these EOS fits is very satisfactory on the whole. The calculated bulk modulus ranges from 440 GPa to 442 GPa, in good agreement with the experimental value of 443 GPa.[30]

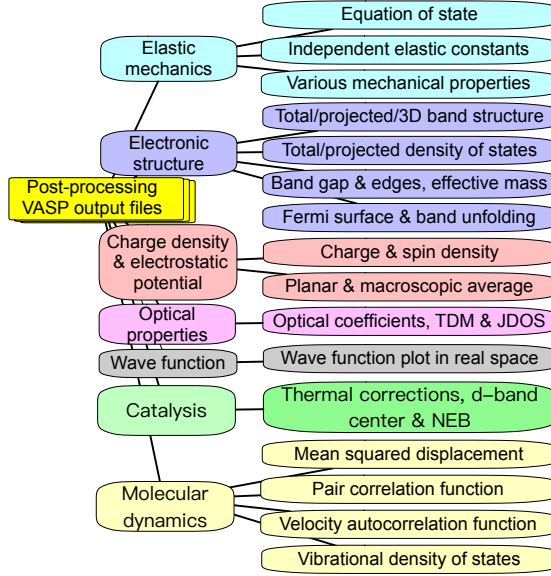


Figure 2: (Color online) A structural overview of the post-processing module implemented into the VASPKIT package.

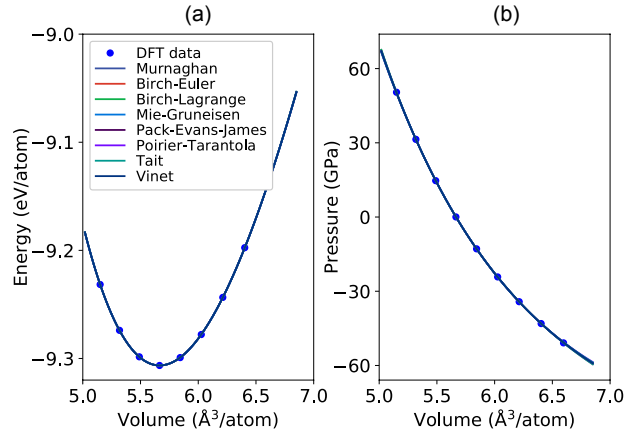


Figure 3: (Color online) Equations of states of diamond using different EOS models as listed in Table 1.

Table 1: The analytic formulae of energy-volume relation, bulk modulus (K) and its pressure derivative (K') for several widely used EOS models [29].

Model	$E(\nu^a)$	$K(\nu = 1)$	$K'(\nu = 1)$	Ref.
Vinet	$E = E_0^b + \frac{BV_0}{C^2} \left(1 - \left(1 + C \left(\nu^{\frac{1}{2}} - 1 \right) \right) e^{-C \left(\nu^{\frac{1}{3}} - 1 \right)} \right)$	$\frac{B}{9}$	$\frac{2}{3}C + 1$	[31]
Tait	$E = E_0 + \frac{BV_0}{C} \left(\nu - 1 + \frac{1}{C} \left(e^{C(1-\nu)} - 1 \right) \right)$	B	$C - 1$	[32]
Poirier-Tarantola	$E = E_0 + BV_0 (\ln(\nu))^2 (3 - C \ln(\nu))$	$6B$	$C + 1$	[33]
Pack-Evans-James	$E = E_0 + \frac{BV_0}{c} \left(\frac{1}{c} \left(e^{3C(1-\nu^{\frac{1}{3}})} - 1 \right) - 3 \left(1 - \nu^{\frac{1}{3}} \right) \right)$	B	$C + 1$	[34]
Murnaghan	$E = E_0 + \frac{BV_0}{(C+1)} \left(\frac{\nu^{-c} - 1}{C} + \nu - 1 \right)$	B	$C + 1$	[35]
Mie-Gruneisen	$E = E_0 + \frac{BV_0}{C} - \frac{BV_0}{C-1} \left(\nu^{-\frac{1}{3}} - \frac{1}{C} \nu^{-\frac{c}{3}} \right)$	$\frac{B}{9}$	$\frac{7+C}{3}$	[36]
Birch (Lagrange)	$E = E_0 + BV_0 C - BV_0 \nu^{\frac{2}{3}} \left((C-2) \left(1 - \nu^{\frac{2}{3}} \right)^2 + C \left(1 - \nu^{\frac{2}{3}} \right) + C \right)$	$\frac{16B}{9}$	$C - 2$	[37]
Birch (Euler)	$E = E_0 + BV_0 \left(\left(\nu^{-\frac{2}{3}} - 1 \right)^2 + \frac{c}{2} \left(\nu^{-\frac{2}{3}} - 1 \right)^3 \right)$	$\frac{8B}{9}$	$C + 4$	[37]

^a $\nu = \frac{V}{V_0}$, where V_0 and V are the volumes at zero and finite pressure respectively.

^b E_0 is the total energy of system at zero pressure.

3.2. Elastic mechanics

The second-order elastic constants play a crucial role in understanding the mechanical and dynamical properties of materials, especially provide information on the stability and stiffness of materials. Within the linear elastic region, the stress σ response of solids to external loading strain ε satisfies the generalized Hooke's law and can be simplified in the Voigt notation,[38]

$$\sigma_i = \sum_{j=1}^6 C_{ij} \varepsilon_j, \quad (4)$$

where strain or stress are represented as a vector with 6 independent components respectively, i.e., $1 \leq i, j \leq 6$, and C_{ij} is the second order elastic stiffness tensor that is expressed by a 6×6 symmetric matrix in units of GPa. The elastic stiffness tensor C_{ij} can be determined based on the first-order derivative of the stress-strain curves proposed by Nielsen and Martin,[39, 40] as expressed in Eq. 4. The number of independent elastic constants depends on the symmetry of crystal. The lower the symmetry means the more the independent elastic constants. For example, the cubic crystals have three but the triclinic ones have 21 independent elastic constants. The classification of the different crystal system with the corresponding number of independent elastic constants for bulk materials are summarized in Table 2. [41, 42, 43]

An alternative theoretical approach to calculate elastic constants is based on the energy variation by applying small strains to the equilibrium lattice configuration.[44] The elastic energy $E_{elastic}(V, \{\varepsilon_i\})$ of a solid under the harmonic approximation is given by

$$\begin{aligned} E_{elastic}(V, \{\varepsilon_i\}) &= E(V, \{\varepsilon_i\}) - E(V_0, 0) \\ &= \frac{V_0}{2} \sum_{i,j=1}^6 C_{ij} \varepsilon_j \varepsilon_i, \end{aligned} \quad (5)$$

where $E(V, \{\varepsilon_i\})$ and $E(V_0, 0)$ are the total energies of the equilibrium and distorted lattice cells, with the volume of V and V_0 , respectively. In the energy-strain method the elastic stiffness tensor is derived from the second-order derivative of the total energy versus strain curves.[44] In general, the stress-strain method requires higher computational precise to achieve the same accuracy as the energy-strain method. Nevertheless, the former requires much smaller set of distortions than the latter.[41, 42, 45, 46, 44] Considering that the energy-strain has less stress sensitivity than the stress-strain one, the former method has been implemented into the VASPKIT package. Meanwhile, the determination of elastic stability criterion is also provided in the elastic utility based on the necessary and sufficient elastic stability conditions in the harmonic approximation[47] for various crystal systems proposed by Mouhat et al.[41, 42, 48]

Table 2: Classification of crystal systems, point group classes and space-group number are provided with the number of independent elastic constants (No. IEC) for bulk materials. In the last column, several prototype materials are shown.

Crystal system	Point groups	Space-groups	No. IEC	Prototype
Triclinic	$1, \bar{1}$	1-2	21	-
Monoclinic	$m, 2, \frac{2}{m}$	3-15	13	ZrO ₂
Orthorhombic	$222, mm2, \frac{2}{m} \frac{2}{m} \frac{2}{m}$	16-74	9	TiS ₂
Tetragonal I	$422, 4mm, 42m, \frac{4}{m} \frac{2}{m} \frac{2}{m}$	89-142	6	MgF ₂
Tetragonal II	$4, \bar{4}, \frac{4}{m}$	75-88	7	CaMoO ₄
Trigonal I	$32, 3m, 3 \frac{2}{m}$	149-167	6	α -Al ₂ O ₃
Trigonal II	$3, \bar{3}$	143-148	7	CaMg(CO ₃) ₂
Hexagonal	$622, 6mm, \bar{6}2m, \frac{6}{m} \frac{2}{m} \frac{2}{m}, 6, \bar{6}, \frac{6}{m}$	168-194	5	Ti
Cubic	$432, \bar{4}3m, \frac{4}{m} \frac{3}{m} \frac{2}{m}, 23, \frac{2}{m} \bar{3}$	195-230	3	Diamond

The flowchart of elastic utility is shown in Fig. 4. First, VASPKIT reads the crystal lattice and atomic positions from the POSCAR file, and then determines the corresponding space-group number; Second, the deformed structures and necessary input files are prepared; Next, the strain energies are calculated for each distorted structure by using VASP package; Then, a polynomial fitting procedure is applied to calculate the second derivative at equilibrium of the energy with respect to the strain; Finally, various mechanical properties such as bulk, shear modulus and Poisson's ratio for polycrystalline materials are determined. For polycrystalline materials, the crystallites are randomly, and such materials can be considered to be quasi-isotropic or isotropic in a statistical sense. Thus, bulk modulus K and shear modulus G are generally obtained by averaging the single-crystal elastic constants. Three of the most widely used averaging approaches have been implemented into the elastic utility: Voigt,[38] Reuss[49]

and Hill[50] schemes. Hill has shown that the Voigt and Reuss elastic moduli are the strict upper and lower bound, respectively.[50] The arithmetic mean of the Voigt and Reuss bounds termed the Voigt-Reuss-Hill (VRH) average is found as better approximation to the actual elastic behavior of a polycrystalline material.

For Voigt bounds are given by the following equations:

$$\begin{cases} 9K_V = (C_{11} + C_{22} + C_{33}) + 2(C_{12} + C_{23} + C_{31}) \\ 15G_V = (C_{11} + C_{22} + C_{33}) - (C_{12} + C_{23} + C_{31}) \\ \quad + 4(C_{44} + C_{55} + C_{66}) \end{cases} \quad (6)$$

while the Reuss bounds are given by:

$$\begin{cases} 1/K_R = (S_{11} + S_{22} + S_{33}) + 2(S_{12} + S_{23} + S_{31}) \\ 15/G_R = 4(S_{11} + S_{22} + S_{33}) - 4(S_{12} + S_{23} + S_{31}) \\ \quad + 3(S_{44} + S_{55} + S_{66}) \end{cases} \quad (7)$$

Voigt and Reuss bounds are rigorous upper and lower bounds of K and G, respectively. Based on Voigt and Reuss bounds, Hill defined $K_{VRH} = 1/2(K_V + K_R)$ and $G_{VRH} = 1/2(G_V + G_R)$, known as the Voigt-Reuss-Hill average is found as better approximation to the actual elastic behavior of a polycrystalline material.[50] According to the values of bulk modulus K and shear modulus G, the Young's modulus E and Poisson's ratio ν can be obtained by $E = \frac{9KG}{3K+G}$ and $\nu = \frac{3K-2G}{2(3K+G)}$, respectively.

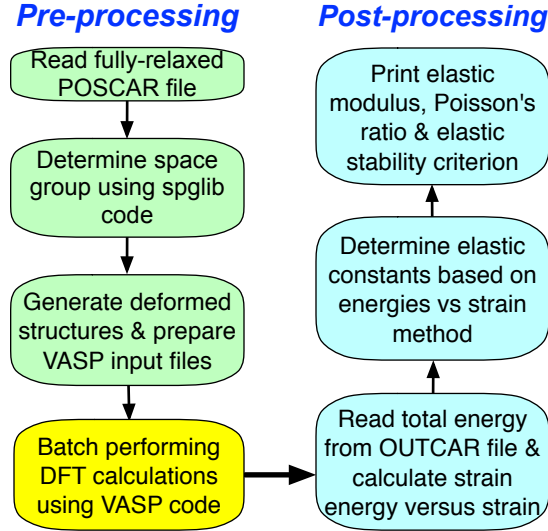


Figure 4: (Color online) Flowchart of the algorithm to determine the second-order elastic constants based on energy-strain method used in the elastic utility.

The relationship of lattice vectors between the distorted and equilibrium lattice cells is given by

$$\begin{pmatrix} \mathbf{a}' \\ \mathbf{b}' \\ \mathbf{c}' \end{pmatrix} = \begin{pmatrix} \mathbf{a} \\ \mathbf{b} \\ \mathbf{c} \end{pmatrix} \cdot (\mathbf{I} + \boldsymbol{\varepsilon}), \quad (8)$$

where \mathbf{I} is the identity matrix. The strain tensor $\boldsymbol{\varepsilon}$ is defined by

$$\boldsymbol{\varepsilon} = \begin{pmatrix} \varepsilon_1 & \frac{\varepsilon_6}{2} & \frac{\varepsilon_5}{2} \\ \frac{\varepsilon_6}{2} & \varepsilon_2 & \frac{\varepsilon_4}{2} \\ \frac{\varepsilon_5}{2} & \frac{\varepsilon_4}{2} & \varepsilon_3 \end{pmatrix}, \quad (9)$$

where ε_i is the six components of the strain $\boldsymbol{\varepsilon}$.

Similarly, the relationship between strain and stress for 2D materials can be given based on the Hooke's law under the in-plane stress condition[41, 51]

$$\begin{bmatrix} \sigma_1 \\ \sigma_2 \\ \sigma_3 \end{bmatrix} = \begin{vmatrix} C_{11} & C_{12} & C_{16} \\ & C_{22} & C_{26} \\ & & C_{66} \end{vmatrix} \cdot \begin{bmatrix} \varepsilon_1 \\ \varepsilon_2 \\ 2\varepsilon_3 \end{bmatrix},$$

where C_{ij} ($i,j=1,2,6$) is the in-plane stiffness tensor. Then the elastic energy can be obtained based on the following formula[52]

$$E_{elastic} = \frac{1}{2}C_{11}\varepsilon_{xx}^2 + \frac{1}{2}C_{22}\varepsilon_{yy}^2 + C_{12}\varepsilon_{xx}\varepsilon_{yy} + 2C_{16}\varepsilon_{xx}\varepsilon_{xy} + 2C_{26}\varepsilon_{yy}\varepsilon_{xy} + 2C_{66}\varepsilon_{xy}^2. \quad (10)$$

Clearly, the C_{ij} is equal to the second partial derivative of strain energy $E_{elastic}$ with respect to strain ε , namely, $C_{ij} = (1/S_0)(\partial^2 E_{elastic}/\partial\varepsilon_i\partial\varepsilon_j)$, where S_0 is the equilibrium area of the system. Therefore, the unit of elastic stiffness tensor for 2D materials is force per unit length (N/m). The classification of the different crystal system with the corresponding number of independent elastic constants and elastic stability conditions for 2D materials are summarized in Table 3.

Table 3: Classification of crystal systems, independent elastic constants, elastic stability conditions for 2D materials [51]. In the last column, several prototype materials are shown.

Crystal system	Independent elastic constants	Elastic stability conditions	Prototype
Oblique	$C_{11}, C_{12}, C_{22}, C_{16}, C_{26}, C_{66}$	$C_{11} > 0$ & $C_{11}C_{22} > C_{12}^2$ & $\det(C_{ij})$	-
Rectangle	$C_{11}, C_{12}, C_{22}, C_{66}$	$C_{11} > 0$ & $C_{66} > 0$ & $C_{11}C_{22} > C_{12}^2$	Borophene
Square	C_{11}, C_{12}, C_{66}	$C_{11} > 0$ & $C_{66} > 0$ & $C_{11} > C_{12} $	SnO
Hexagonal	C_{11}, C_{12}	$C_{11} > 0$ & $C_{11} > C_{12} $	Graphene, MoS ₂

As a benchmark test, we list the calculated the second-order elastic constants for 2D and bulk prototype materials belonging to different crystal systems in Tables 4 and 5 respectively, together with other theoretical values [42, 53, 54, 55] for verification purposes. It is found that the results produced with different codes based on total-energy calculations, are in good agreement with each other.

Table 4: Elastic stiffness constants (in units of GPa) for ZrO₂, TiS₂, MgF₂, CaMoO₄, α -Al₂O₃, CaMg(CO₃)₂, Ti and Diamond. For comparison purposes, the available theoretical values from the previous literature are also shown [42].

C_{ij}	ZrO ₂		TiS ₂		MgF ₂		CaMoO ₄		α -Al ₂ O ₃		CaMg(CO ₃) ₂		Ti		Diamond	
	Calc.	Ref.	Calc.	Ref.	Calc.	Ref.	Calc.	Ref.	Calc.	Ref.	Calc.	Ref.	Calc.	Ref.	Calc.	Ref.
C_{11}	334	334	314	312	134	130	130	126	452	451	192	194	184	189	1051	1052
C_{12}	155	151	29	28	80	78	53	58	149	151	64	67	83	85	127	125
C_{13}	82	82	78	84	59	55	47	46	108	108	54	57	78	74		
C_{14}									20	21	17	18				
C_{15}	26	32									13	12				
C_{16}					10	10										
C_{22}	352	356	311	306												
C_{23}	146	142	25	21												
C_{24}																
C_{25}	5	2														
C_{26}																
C_{33}	263	251	404	406	192	185	112	110	455	452	107	108	197	187		
C_{34}																
C_{35}	2	7														
C_{36}																
C_{44}	78	71	73	73	52	61	30	29	133	132	37	39	46	41	560	559
C_{45}																
C_{46}	15	15														
C_{55}	70	71	100	106												
C_{56}																
C_{66}	113	115	118	117	90	83	38	34								

3.3. Band Structure and Density of States

In order to plot band structure, one need to define a set of k -paths across the specified high-symmetry points in the first Brillouin zone. The k -path utility is able to automatically generate the suggested k -paths for a given crystal structure based on the algorithm proposed by Hinuma et al[24] for bulk [24] and 2D materials[56]. The VASPKIT also provides the python script to visualize the recommended k -paths in the first Brillouin zone using

Table 5: In-plane elastic stiffness constants (in units of N/m) for Graphene, MoS₂, SnO and Phosphorene. For comparison purposes, the available theoretical or experimental values from the previous literature are also shown.

Systems	C ₁₁		C ₂₂		C ₁₂		C ₆₆	
	Our work	Literature	Our work	Literature	Our work	Literature	Our work	Literature
Graphene	349.1	358.1 [53]			60.3	60.4 [53]		
MoS ₂	128.9	131.4 [54]			32.6	32.6 [54]		
SnO	48.14				38.9		39.0	
Phosphorene	104.4	105.2 [55]	34.0	26.2 [55]	21.6	18.4 [55]	27.4	

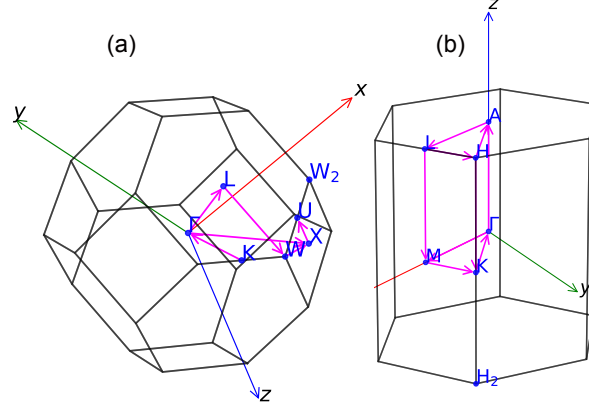


Figure 5: (Color online) First Brillouin zone, special high symmetry points, and recommended k -paths for (a) face-centered cubic and hexagonal close packed lattices respectively.

Matplotlib plotting library.[57] The figure 5 shows the recommended k -paths of face-centered cubic and hexagonal lattices.

As illustrated examples, the projected band structures and density of states (DOS) of BiClO (P4/nmm) and graphene monolayers are depicted in Fig. 6. The global band structures of the highest valence and lowest conduction band for MoTe₂ ($P\bar{6}m2$) and BiIO (P4/nmm) are also shown in Fig. 7, to investigate the band dispersion anisotropy of 2D materials.

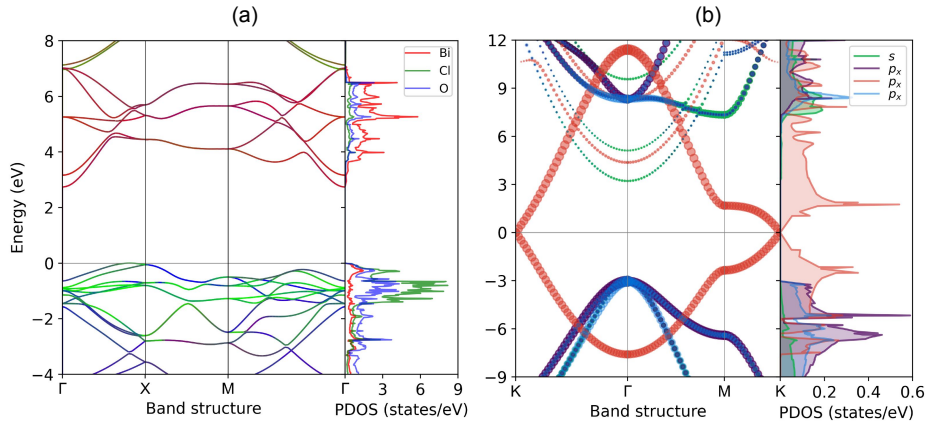


Figure 6: (Color online) Projected band structure (left panel) and density of states (right panel) of (a) BiClO (P4/nmm) and (b) graphene monolayers. The Fermi energy is set to zero eV.

3.4. Effective Masses of Carriers

Generally, the band dispersions close to conduction or valence band extrema can be approximated as parabolic for the semiconductors with low carrier concentrations. Consequently, the analytical expression of effective masses of carriers (EMC) m^* for electrons and holes (in units of electron mass m_0) is given by

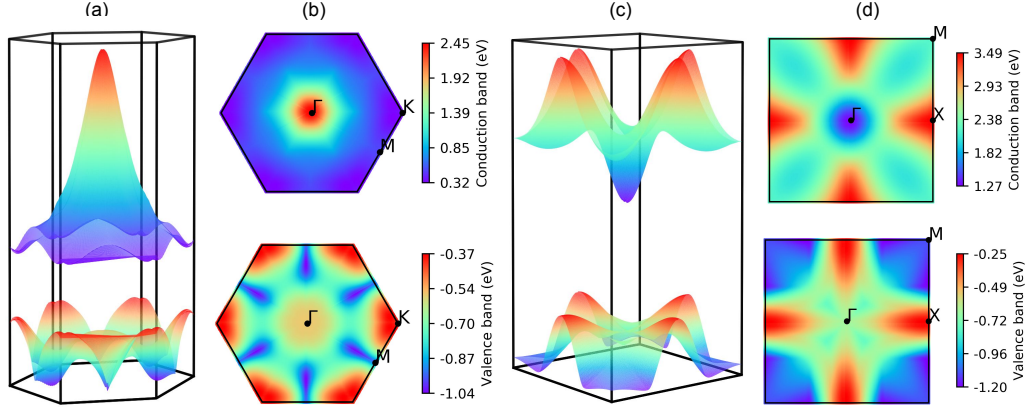


Figure 7: (Color online) Global band structures of the highest valence and lowest conduction band for (a) MoTe₂ ($P\bar{6}m2$) and (b) BiIO ($P4/nmm$) monolayers. The Fermi energy is set to zero.

$$m^* = \hbar^2 \left[\frac{\partial^2 E(k)}{\partial^2 k} \right]^{-1}, \quad (11)$$

where $E(k)$ are the energy dispersion relation functions described by band structures, and \hbar is the reduced Planck constant. Clearly, m^* is inversely proportional to the curvature of the electronic dispersion in reciprocal space, implying that CB and VB edges with larger dispersions result in smaller effective masses. It is noteworthy that the expression presented above should be not used in the some cases of the non-parabolic band dispersion relations, for example, the linear dispersion near the band edges of graphene.[58] Similarly, the Fermi velocity represents the group velocity of electrons traveling in the material, defined as

$$v_F = \frac{1}{\hbar} \frac{\partial E}{\partial k}. \quad (12)$$

Figure 8 illustrates schematically the determination of effective masses by fitting the band dispersion relation using a second order polynomial. The effective masses of carriers are calculated based on an ultrafine k -mesh of density uniformly distributed inside a circle of radius (k -cutoff). Haastrup *et al.* pointed that the inclusion of third order terms stabilizes the fitting procedure and yields the effective masses that are less sensitive to the details of the employed k -point grids.[54] Thus, a third order polynomial is also adopted to fit the band energy curvature in the EMC utility.

Table 6: Effective masses of electron m_e and hole m_h carriers (in units of the electron mass m_0) for typical semiconductors using PBE approach. The masses are labeled by the band extremum and the direction of the high symmetry line along which the mass is calculated using a simple parabolic line fit. The labels of high-symmetry points are adopted from the Ref. [24].

Systems	Label	m_e	m_h	Label	m_e	m_h	Ref.
Phosphorene	Γ -X	1.23	7.21	Γ -Y	0.19	0.17	[54]
MoS ₂ monolayer	K- Γ	0.47	0.56	K-M	0.52	0.69	[54]
GaAs bulk	Γ -X	0.06	0.35	Γ -L	0.06	0.81	[59]
ZnO bulk	Γ -A	0.14	2.88	Γ -M	0.14	0.32	[60]
Diamond bulk	Γ -X	0.32	0.27	Γ -L	0.26	0.69	[61]

In Table 6 we shows the calculated effective masses for several typical 2D and 3D semiconductors with available effective mass data, including Phosphorene[54], MoS₂[54], GaAs[59], ZnO[60] and Diamond[61]. Overall, the agreement is very satisfactory. In addition, the EMC utility can also calculate the orientation-dependent effective masses of charge carriers. Examples for this functionality are shown in Fig. 9. One can find that the calculated effective masses of two investigated systems show a strong anisotropy character, especially for the case of bulk Si.

3.5. Charge Density and Potential Manipulation

For the magnetic systems, the charge density $\rho(\mathbf{r})$ and magnetization (spin) density $m(\mathbf{r})$ are defined as

$$\begin{aligned} \rho(\mathbf{r}) &= \rho_{\uparrow}(\mathbf{r}) + \rho_{\downarrow}(\mathbf{r}) \\ m(\mathbf{r}) &= \rho_{\uparrow}(\mathbf{r}) - \rho_{\downarrow}(\mathbf{r}), \end{aligned} \quad (13)$$

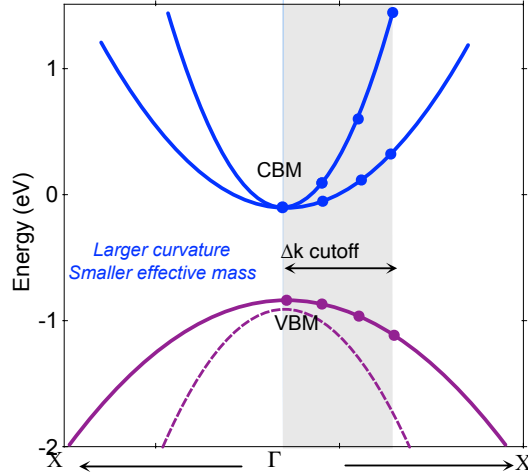


Figure 8: (Color online) Schematic illustration of the determination of effective masses based on second-order polynomial fitting around the conduction and valence band extrema.

where $\rho_{\uparrow}(\mathbf{r})$ and $\rho_{\downarrow}(\mathbf{r})$ are the spin-up and spin-down density. The spin density $\rho_{\sigma}(\mathbf{r})$ is expressed as

$$\rho_{\sigma}(\mathbf{r}) = \sum_{occ} \varphi_{i\sigma}^*(\mathbf{r})\varphi_{i\sigma}(\mathbf{r}), \quad (14)$$

where σ and i are the spin- and band-index respectively. $\varphi_{i\sigma}(\mathbf{r})$ is the normalized single-particle wave-function and *occ* means that be summed over all occupied states.

The charge density difference $\Delta\rho(\mathbf{r})$ can track the charge transfer to get an idea of such as what is interacting with what in the system and how strongly. The $\Delta\rho(\mathbf{r})$ can be obtained

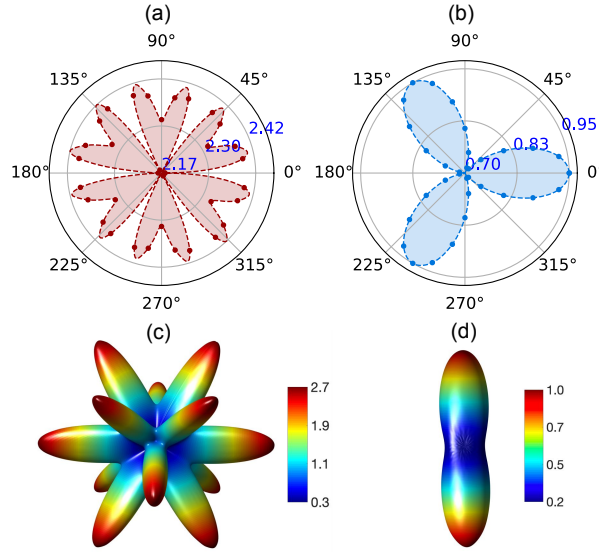


Figure 9: (Color online) Orientation-dependent effective masses (in units of electron mass m_0) of (a, c) hole and (b, d) electron carriers for 2D BN monolayer (a, b) and bulk Si (c, d) respectively.

$$\Delta\rho(\mathbf{r}) = \rho_{AB}(\mathbf{r}) - \rho_A(\mathbf{r}) - \rho_B(\mathbf{r}), \quad (15)$$

where $\rho_A(\mathbf{r})$, $\rho_B(\mathbf{r})$ and $\rho_{AB}(\mathbf{r})$ are the charge density of A and B reactants, and C product. VAPSKIT package can extract charge-, spin-density, electrostatic potential as well as the difference of these quantities, and save as VESTA (.vasp)[14, 15, 62], XCrysDen (.xsf) [26], or Gaussian (.cube) formats [63].

From the three-dimensional electronic charge density and electrostatic potential one can get the average one-dimensional charge density $\bar{n}(z)$ and electrostatic potential $\bar{V}(z)$ by calculating the planar average function (f):[64]

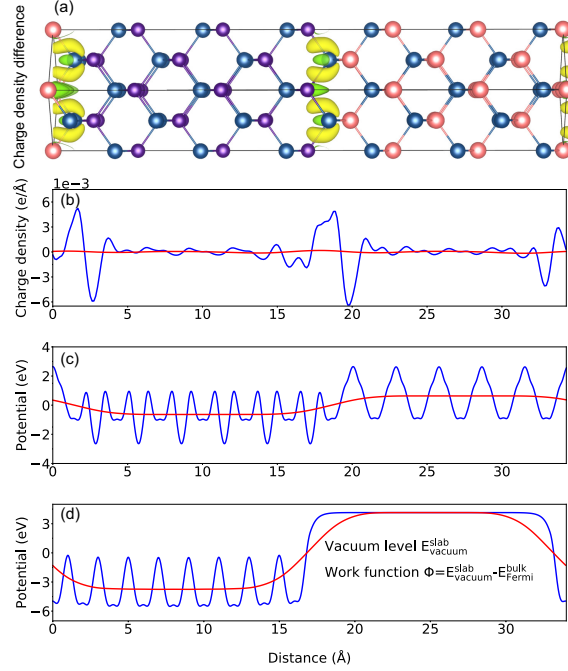


Figure 10: (Color online) (a) Charge density difference, planar- (blue line) and macroscopic averages (red line) of (b) charge density difference, (c) electrostatic potential of a GaAs/AlAs (100) heterojunction, and (d) electrostatic potential of a GaAs (110) slab. Ga, As, Al atoms are shown in purple, blue, red respectively.

$$\bar{f}(z) = \frac{1}{S} \int_S V(\mathbf{r}) dx dy, \quad (16)$$

where S represents the area of a unit cell in the $x - y$ plane. Generally, this planar-averaged charge density and potential exhibit periodic oscillations along the z axis due to the spatial distribution of the electrons and ionic cores. These oscillations can be removed using a macroscopic averaging procedure:[64]

$$\bar{\bar{f}}(z) = \frac{1}{L} \int_{-L/2}^{L/2} \bar{f}(z) dz, \quad (17)$$

where L is the length of the period of oscillation along z . By definition, this macroscopic average would produce a constant value in the bulk. It is expected that reaches a plateau value in the bulk-like regions of each layer in the superlattice. As an example, figure 10 shows the calculated planar and macroscopic averages of charge density difference and electrostatic potential for a (100)-oriented GaAs/AlAs heterojunction and a (110)-oriented GaAs slab, respectively. The vacuum level, work function, ionization energy, electron affinity, potential alignment, which are parameters of great importance for any electronic material, can be determined as illustrated in Fig. 11.[65]

3.6. Band Structure Unfolding

The electronic structures of real materials are perturbed by various structural defects, impurities, fluctuations of the chemical composition, and etc. In DFT calculations, these defects and incommensurate structures are usually investigated by using supercell (SC) models. However, interpretation of $E(\mathbf{k})$ versus \mathbf{k} band structures is most effective within the primitive cell (PC). Popescu and Zunger proposed the effective band structures (EBS) method which can unfold the band structure of supercell Brillouin zone (SBZ) into the corresponding primitive cell Brillouin zone (pbz).[66, 67] Such band unfolding techniques greatly simplify the analysis of the results and enable direct comparisons with experimental measurements, for example, angle-resolved photoemission spectroscopy (ARPES) often represented along the high-symmetry directions of the primitive cell BZ. The lattice vectors of the SC and PC satisfy $\mathbf{A} = M \cdot \mathbf{a}$, where \mathbf{A} and \mathbf{a} are the lattice vectors of SC and PC. The elements of transformation matrix M are integers ($m_{ij} \in \mathbb{Z}$) when building SC from PC. As a general convention, capital and lower case letters indicate the quantities in the SC and PC respectively unless otherwise stated. A similar relation holds in reciprocal space:

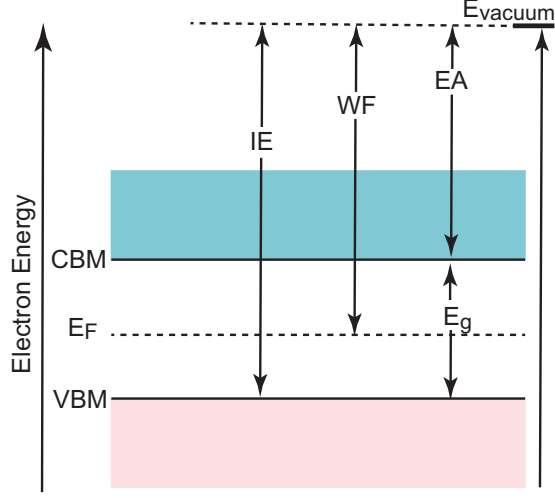


Figure 11: (Color online) Schematic diagram of the definition of vacuum level E_{vacuum} , work function WF , energy gap E_g , Band edges (CBM and VBM), ionization energy IE and electron affinity EA .

$$\begin{pmatrix} \mathbf{B}_1 \\ \mathbf{B}_2 \\ \mathbf{B}_3 \end{pmatrix} = M^{-1} \cdot \begin{pmatrix} \mathbf{b}_1 \\ \mathbf{b}_2 \\ \mathbf{b}_3 \end{pmatrix}, \quad (18)$$

The reciprocal lattice vectors \mathbf{g}_n (\mathbf{G}_n) in the pbz (SBZ) expressed as

$$\begin{aligned} \mathbf{g}_n &= \sum_i n_i \mathbf{b}_i, \quad n_i \in \mathbb{Z} \\ \mathbf{G}_n &= \sum_i m_i \mathbf{B}_i, \quad m_i \in \mathbb{Z} \end{aligned},$$

where $\{\mathbf{g}_n\} \subset \{\mathbf{G}_n\}$, i.e., every reciprocal lattice vector of the pbz is also one of the SBZ.

For a given \mathbf{k} in pbz, there is a \mathbf{K} in the SBZ to which it folds into, and the two vectors are related by a reciprocal lattice vector \mathbf{G} in the SBZ:

$$\mathbf{k} = \mathbf{K} + \mathbf{G}_i, \quad i = 1, \dots, N_{\mathbf{K}}, \quad (19)$$

where $N_{\mathbf{K}} = \det M$ is the multiplicity of the supercell. When choosing plane waves as basis functions, the individual weights of unfolded \mathbf{k} points are expressed as

$$\begin{aligned} P_{\mathbf{K}m}(\mathbf{k}_j) &= \sum_{\mathbf{g}} |C_{\mathbf{K}m}(\mathbf{g} + \mathbf{k}_j - \mathbf{K})|^2 \\ &= \sum_{\mathbf{g}} |C_{\mathbf{K}m}(\mathbf{g} + \mathbf{G}_i)|^2 \end{aligned}, \quad (20)$$

where $C_{\mathbf{K}m}$ is the plane wave coefficients of the eigenstate $|\mathbf{K}m\rangle$ and m is band index. The sum now runs over the reciprocal lattice vectors of the primitive cell \mathbf{g} . Clearly, all the filtered $C_{\mathbf{K}m}(\mathbf{g} + \mathbf{G}_j)$ coefficients only contribute to the spectral function. As an illustrated example, we present the orbital-projected effective band structure of 4×4 MoS₂ supercell with a neutral sulfur vacancy in Fig. 12. One can found that two almost degenerated defect states which are derived from Mo- d_{x^2} states with some mixing of S- p_y reside within the fundamental band gap of MoS₂, showing a stronger localized character. Furthermore, the Bloch character close to the valence band edge is perturbed by the presence of the sulfur vacancy.

3.7. Linear Optical Properties

The linear optical properties of semiconductors can be obtained from the frequency-dependent complex dielectric function $\varepsilon(\omega)$

$$\varepsilon(\omega) = \varepsilon_1(\omega) + i\varepsilon_2(\omega) \quad (21)$$

where $\varepsilon_1(\omega)$ and $\varepsilon_2(\omega)$ are the real and imaginary parts of the dielectric function, and ω is the photon frequency. Within the one-electron picture, the imaginary part of the dielectric function $\varepsilon_2(\omega)$ is obtained from the following equation:[68]

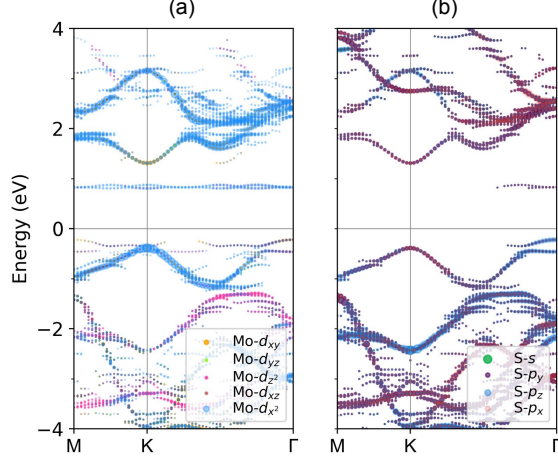


Figure 12: (Color online) Orbital-projected effective band structure of (a) Mo and (b) S in a 4×4 MoS₂ supercell unfolded into the primitive-cell Brillouin zone based on Eq. 20. The Fermi energy is set to zero.

$$\varepsilon_2(\omega) = \frac{4\pi^2 e^2}{\Omega} \lim_{q \rightarrow 0} \frac{1}{q^2} \times \sum_{c,v,\mathbf{k}} 2w_{\mathbf{k}} \delta(E_c - E_v - \omega) |\langle c | \mathbf{e} \cdot \mathbf{q} | v \rangle|^2, \quad (22)$$

where $\langle c | \mathbf{e} \cdot \mathbf{q} | v \rangle$ is the integrated optical transitions from the valence states (v) to the conduction states (c), \mathbf{e} is the polarization direction of the photon and \mathbf{q} is the electron momentum operator. The integration over the \mathbf{k} is performed by summation over special k -points with a corresponding weighting factor $w_{\mathbf{k}}$. The real part of the dielectric function $\varepsilon_1(\omega)$ is obtained from the imaginary part $\varepsilon_2(\omega)$ based on the usual Kramers-Kronig transformation

$$\varepsilon_1(\omega) = 1 + \frac{2}{\pi} P \int_0^\infty \frac{\varepsilon_{\alpha\beta}^{(2)}(\omega') \omega'}{\omega^2 - \omega'^2 + i\eta} d\omega', \quad (23)$$

where P denotes the principle value and η is the complex shift parameter. The frequency-dependent linear optical spectra, e.g., refractive index $n(\omega)$, extinction coefficient $\kappa(\omega)$, absorption coefficient $\alpha(\omega)$, energy-loss function $L(\omega)$, and reflectivity $R(\omega)$ can be calculated from the real $\varepsilon_1(\omega)$ and the imaginary $\varepsilon_2(\omega)$ parts:[69]

$$n(\omega) = \left[\frac{\sqrt{\varepsilon_1^2 + \varepsilon_2^2} + \varepsilon_1}{2} \right]^{\frac{1}{2}}, \quad (24)$$

$$k(\omega) = \left[\frac{\sqrt{\varepsilon_1^2 + \varepsilon_2^2} - \varepsilon_1}{2} \right]^{\frac{1}{2}}, \quad (25)$$

$$\alpha(\omega) = \frac{\sqrt{2}\omega}{c} \left[\sqrt{\varepsilon_1^2 + \varepsilon_2^2} - \varepsilon_1 \right]^{\frac{1}{2}}, \quad (26)$$

$$L(\omega) = \text{Im} \left(\frac{-1}{\varepsilon(\omega)} \right) = \frac{\varepsilon_2}{\varepsilon_1^2 + \varepsilon_2^2}, \quad (27)$$

$$R(\omega) = \frac{(n-1)^2 + k^2}{(n+1)^2 + k^2}. \quad (28)$$

In Fig. 13 we present the linear optical spectra of silicon as determined by solving the Bethe-Salpeter Equation (BSE) on the top of G_0W_0 approximation. One can find that the absorption coefficient become significant only after 3.0 eV. This is because silicon has an indirect band gap, resulting in a low absorption coefficient in the visible

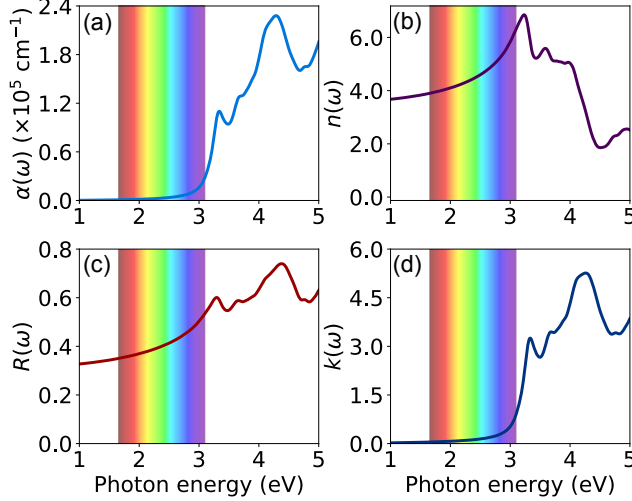


Figure 13: (Color online) G_0W_0 -BSE calculated (a) absorption coefficient, (b) refractive index, (c) reflectivity and (d) extinction coefficient of silicon.

region. Since the GW approximation can correct the one electron eigenvalues obtained from DFT within a many-body quasiparticle framework, including the exchange and correlation effects in a self-energy term dependent on the one particle Green's function G and the dynamically screened Coulomb interaction W .^[70, 71] Furthermore, the errors originating from the lack of ladder diagrams in determining W can be included through solution of the Bethe-Salpeter equation (BSE).^[72] It would be expected that the GW-BSE calculated optical properties yield better agreement with experimental values. In the single-shot G_0W_0 approximation, the one-electron Green's function G is self-consistently updated within a single iteration, while the screened Coulomb interaction W is fixed at its initial value.

It should be pointed that the formulae (24-28) may not hold true for low-dimensional materials since the dielectric function is not straightforward and depends on the thickness of the vacuum layer when the low-dimensional systems are simulated using a periodic stack of layers with sufficiently large interlayer distance L to avoid artificial interactions between the periodic images of the 2D sheet crystals in the standard DFT calculations.^[73, 74] To avoid the thickness problem, the optical conductivity $\sigma_{2D}(\omega)$ is used to characterize the optical properties of 2D sheets. Based on the Maxwell equation, the 3D optical conductivity can be expressed as^[75]

$$\sigma_{3D}(\omega) = i[1 - \varepsilon(\omega)]\varepsilon_0\omega \quad (29)$$

where $\varepsilon(\omega)$ is frequency-dependent complex dielectric function given in (21), ε_0 is the permittivity of vacuum and ω is the frequency of incident wave. The in-plane 2D optical conductivity is directly related to the corresponding $\sigma_{3D}(\omega)$ component through the equation^[75, 76]

$$\sigma_{2D}(\omega) = L\sigma_{3D}(\omega) \quad (30)$$

where L is the slab thickness in the simulation cell. One can easily note that expression (30) is independent of L . The normalized reflectance $R(\omega)$, transmittance $T(\omega)$ and absorbance $A(\omega)$ are independent of the light polarization for a freestanding 2D crystal sheet when normal incidence is assumed,^[75, 76]

$$\begin{aligned} R &= \left| \frac{\tilde{\sigma}/2}{1 + \tilde{\sigma}/2} \right|^2 \\ T &= \frac{1}{|1 + \tilde{\sigma}/2|^2} \\ A &= \frac{\text{Re } \tilde{\sigma}}{|1 + \tilde{\sigma}/2|^2} \end{aligned} \quad (31)$$

where $\tilde{\sigma}(\omega) = \sigma_{2D}(\omega)/\varepsilon_0c$ is the normalized conductivity (c is the speed of light). Since the interband contribution is only considered, the formula (31) is valid for semiconducting and insulating 2D crystals with restriction of $A + T + R = 1$. Generally, the reflectance of 2D sheets is extremely small and the absorbance can be approximated

by the real part of $\tilde{\sigma}(\omega)$, namely, $A(\omega) = \text{Re } \sigma_{2D}(\omega)/\varepsilon_0 c$. To demonstrate this functionality, the PBE-calculated linear optical spectra of freestanding graphene and phosphorene monolayers are displayed in Fig. 14. Our results are in good agreement with the available theoretical optical curves.[75, 76, 77]

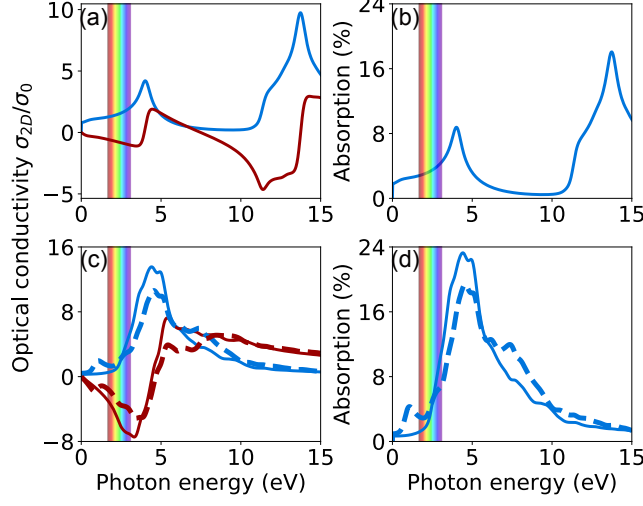


Figure 14: (Color online) Real (blue line) and imaginary (red line) parts of frequency-dependent optical conductivity $\sigma_{2D}(\omega)$ for (a) graphene and (c) phosphorene [in units of $\sigma_0 = e^2/(4\hbar)$]. Absorption spectra $A(\omega)$ of (b) graphene and (d) phosphorene. The incident light polarized along the armchair and zigzag directions of phosphorene are presented by solid and dashed lines respectively.

3.8. Joint Density of States

For a semiconductor, the optical absorption in direct band-to-band transitions is proportional to [78]

$$\frac{2\pi}{\hbar} \int_{\text{BZ}} |\langle v | \mathcal{H}' | c \rangle|^2 \frac{2}{(2\pi)^3} \delta(E_c(\mathbf{k}) - E_v(\mathbf{k}) - \hbar\omega) d^3k,$$

where \mathcal{H}' is the perturbation associated with the light wave and $\langle v | \mathcal{H}' | c \rangle$ is the transition matrix from states in the valence band (VB) to states in the conduction band (CB); δ is the Dirac delta function which switches on this contribution when a transition occurs from one state to another, i.e., $E_c(\mathbf{k}) - E_v(\mathbf{k}) = \hbar\omega$. The factor 2 stems from the spin degeneracy. The integration is over the entire Brillouin zone (BZ). The matrix elements vary little within the BZ; Therefore, we can pull these out in front of the integral and obtain

$$\frac{2\pi}{\Omega\hbar} |\langle v | \mathcal{H}' | c \rangle|^2 \cdot \int \frac{2\Omega}{(2\pi)^3} \delta(E_c(\mathbf{k}) - E_v(\mathbf{k}) - \hbar\omega) d^3k,$$

where Ω is the volume of the lattice cell, and the factor $\Omega/(2\pi)^3$ normalizes the \mathbf{k} vector density within the Brillouin zone. The second term is the joint density of states (JDOS). After sum over all states within the first Brillouin zone and all possible transitions initiated by photons with a certain energy $\hbar\omega$ between valence and conduction bands, we obtain

$$\begin{aligned} j(\omega) &= \sum_{v,c} \frac{\Omega}{4\pi^3} \int d^3\mathbf{k} \delta(E_c(\mathbf{k}) - E_v(\mathbf{k}) - \hbar\omega) \\ &= 2 \sum_{v,c,\mathbf{k}} w_{\mathbf{k}} \delta(E_c(\mathbf{k}) - E_v(\mathbf{k}) - \hbar\omega), \end{aligned} \quad (32)$$

where c and v belong respectively to the valence and conduction bands, $E(\mathbf{k})$ are the eigenvalues of the Hamiltonian, and $w_{\mathbf{k}}$ are weighting factors.

The Dirac Delta function in Eq. 32 can be numerically approximated by means of such as Gaussian function normalized to one:

$$G(\omega) = \frac{1}{\sigma\sqrt{2\pi}} e^{-(E_{\mathbf{k},n'} - E_{\mathbf{k},n} - \hbar\omega)^2 / 2\sigma^2}, \quad (33)$$

where σ is the broadening parameter. To demonstrate this functionality, we show the calculated total and partial JDOS for $\text{CH}_3\text{NH}_3\text{PbI}_3$ and Si in Fig. 15. The total JDOS include all possible interband transitions from all the valence to all the conduction bands according to Eq. 32; while the partial JDOS consider only the interband transitions from the highest valence band to the lowest conduction one.

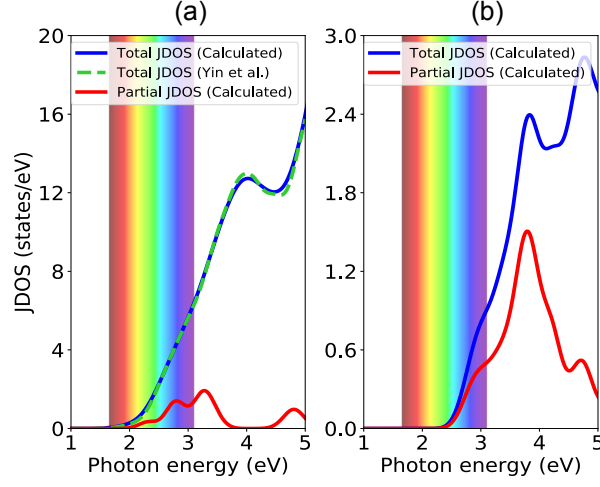


Figure 15: (Color online) Calculated joint density of states for (a) $\text{CH}_3\text{NH}_3\text{PbI}_3$ and (b) Si. Blue and purple lines represent the total and partial joint density of states respectively. Adapted with permission from Ref. [79]. Copyright 2014 WILEY-VCH Verlag GmbH & Co. KGaA.

3.9. Transition Dipole Moment

The transition dipole moment (TDM) or dipole transition matrix elements is the electric dipole moment associated with a transition between an initial state a and a final state b , as denoted as $P_{a \rightarrow b}$:[\[80\]](#)

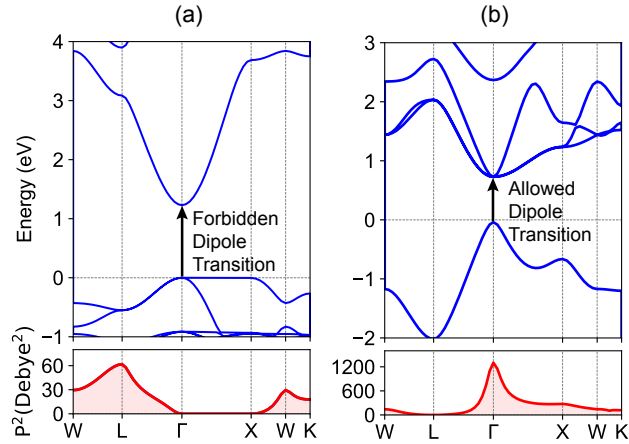


Figure 16: (Color online) Calculated band structure (top panel) and transition dipole moment (bottom panel) for (a) $\text{Cs}_2\text{AgInCl}_6$ and (b) $\text{Cs}_2\text{InBiCl}_6$.

$$P_{a \rightarrow b} = \langle \psi_b | \mathbf{r} | \psi_a \rangle = \frac{i\hbar}{(E_b - E_a) m} \langle \psi_b | \mathbf{p} | \psi_a \rangle, \quad (34)$$

where ψ_a and ψ_b are energy eigenstates with energy E_a and E_b ; m is the mass of the electron. When choosing plane waves as basis functions, the $P_{a \rightarrow b}$ is further expressed as

$$P_{a \rightarrow b} = \frac{\hbar^2}{(E_b - E_a) m} \sum_i C_{ai} C_{bi}^* G_i, \quad (35)$$

where C_a, C_b and \mathbf{G} are plane-wave coefficients and reciprocal space vector with the same \mathbf{k} vector, respectively, summed over the the number of plane-waves. In general the TDM is a complex vector quantity that includes the phase factors associated with the two states. Its direction gives the polarization of the transition, which determines how the system will interact with an electromagnetic wave of a given polarization, while the sum of the squares of TDM, P^2 give the transition probabilities between to states.

In Fig. 16 we provide some specific examples to illustrate its use. It is seen that the calculated TDM amplitude is zero for transition between the conduction band minimum (CBM) and valence band maximun (VBM) at the Γ point, implying no optical absorption between these two states. On the other hand, the excellent optical absorption between CBM and VBM is predicted when all Ag is substituted by Bi atom.[81] The calculated results by VASPKIT is good agreement with previous theoretical report.

3.10. Fermi surface

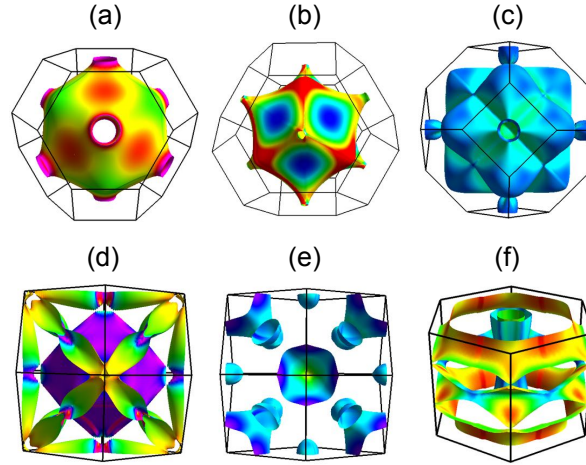


Figure 17: (Color online) Calculated Fermi surface of (a) Cu, (b) spin up for Ni, (c) spin down for Ni, (d) spin up for Fe, (e) spin up down Fe and (f) MgB₂ respectively, visualized by the FermiSurfer package[82].

The physical properties of metals are determined by electrons occupying states near the Fermi energy, the knowledge of these states - especially the density of states at the Fermi energy and the characteristic features of the Fermi surface. The topology of Fermi surface is also related with superconductivity, electronic topological transitions, spin density wave, charge-density waves.[83] Several examples of Fermi surface are shown in Fig. 17.

3.11. Wave Functions Visualization in Real Space

To visualize wave functions plots, VASPKIT package first reads the plane wave function $\psi_{i,\mathbf{k}}(\mathbf{k})$ coefficients of the specified wave-vector \mathbf{k} point and band-index n from the WAVECAR file, and performs a fast Fourier transform algorithm to convert the $\psi_{i,\mathbf{k}}(\mathbf{k})$ from the reciprocal space to the real space, as denoted by $\psi_{i,\mathbf{k}}(\mathbf{r})$. The $\psi_{i,\mathbf{k}}(\mathbf{r})$ can thus be obtained

$$\psi_{i,\mathbf{k}}(\mathbf{r}) = \frac{1}{\sqrt{\Omega}} \sum_{\mathbf{G}} C_{i,\mathbf{k}+\mathbf{G}} e^{i(\mathbf{k}+\mathbf{G})\cdot\mathbf{r}}, \quad (36)$$

where $C_{i,\mathbf{k}+\mathbf{G}}$ is the plane-wave coefficient of the wave vector \mathbf{k} in reciprocal space. Examples of the calculated wave function plots in real space are shown in Fig. 18.

3.12. *d*-Band Center

The *d*-band center model of Hammer and Nørskov is widely used in understanding and predicting catalytic activity on transition metal surfaces. The chief principle underlying the theory is that the binding energy of an adsorbate to a metal surface is largely dependent on the electronic structure of the surface itself. In this model, the band of *d*-states participating in the interaction is approximated by the center of the *d*-band, as denoted by ε_d : [84]

$$\varepsilon_d = \frac{\int_{-\infty}^{\infty} n_d(\varepsilon) \varepsilon d\varepsilon}{\int_{-\infty}^{\infty} n_d(\varepsilon) d\varepsilon}, \quad (37)$$

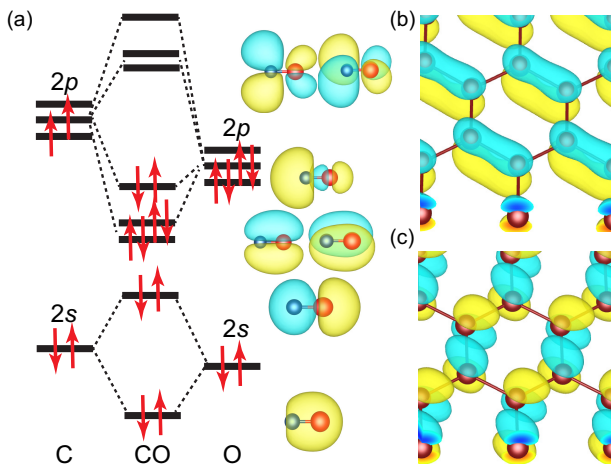


Figure 18: (Color online) Calculated isosurfaces of wave functions in real space for (a) CO molecule, (b) VBM and (c) CBM for graphene respectively, visualized by the VESTA package [[62]].

where n_d and ε are projected-DOS and energy of transition metal d states. According to this model, the adsorption energy on transition metal surface correlates the upward shift of d -band center with respect to the Fermi energy. A stronger upward shift indicates the possibility of the formation of a larger number of empty anti-bonding states, leading to a stronger binding energy.[85, 86, 84] It may be worth mentioning here that the position of d -band center linearly upshifts with increasing the number of empty states above the Fermi level. Therefore, one can specify the integral upper limit in Eq. 37 to calculate d -band center by using VASPKIT code.

3.13. Thermo Energy Correction

Gibbs free energy plays a crucial role in catalysis reaction. The equations used for calculating thermochemical data for gas in VASPKIT is equivalent to those in Gaussian program.[87, 88] The Gibbs free energy G is given by

$$G = H - TS, \quad (38)$$

where H , T and S represent enthalpy, temperature and entropy respectively. The enthalpy H in Eq. 38 can be written as $H = U + k_B T$, where k_B is Boltzmanns constant. Both internal thermal energy U and entropy S have included the contributions from translational, electronic, rotational and vibrational motions as well as zero-point energy (ZPE) of molecules. Moreover, to calculate correctly when the number of moles (labeled N) of gas changes during the course of a reaction, the Gibbs free energy has also included $\Delta PV = \Delta NRT$, where R is molar gas constant. It is worth mentioning that only the modes with real vibrational frequencies are considered and the model with imaginary one are ignored during the calculations of the vibration contributions. Specifically, for linear (non-linear) molecules containing n atoms, the degree of vibrational freedom is $3n - 5$ ($3n - 6$). VASPKIT will neglect the smallest 5 (6) frequencies. We take oxygen molecular as an example to calculate its free energy at 298.15 K using the corrected algorithm mentioned above. It is found that the calculated correction to free energy of O_2 molecule is -0.4467 eV, which is very close to the experimental data of -0.4468 eV at 298.15 K and normal atmospheric pressure.[89] And the thermo correction result from VASPKIT is exactly same with that from Gaussain program by setting same molecular structure and frequencies.

Unlike gas molecules, when the adsorbed molecules form chemical bonds with substrate, their translational and rotational freedom will be constrained. Consequently, the contributions from translation and rotation to entropy and enthalpy are significantly reduced turn into vibrational modes (at least at low temperatures-at higher temperatures, they might become frustrated translational or frustrated rotational). One common method is to attribute the translational or rotational part of the contribution to vibration, that is, the $3n$ vibrations of the surface-adsorbing molecules (except the imaginary frequency) are all used to calculate the correction of the thermo energy.[84] Considering that a small vibration mode makes a large contribution to entropy. It is very likely that a small vibration frequency will lead to abnormal entropy and free energy correction. Thus, VASPKIT allows to specify a threshold value which defines the lower limit of frequencies. For example, if a threshold value of 50 cm^{-1} is adopted, implying that the frequencies below 50 cm^{-1} are approximately equal to 50 cm^{-1} during the calculations of the vibration contributions to the adsorbed molecular free energy correction.

3.14. Molecular Dynamics

The molecular dynamics (MD) describe that how the atoms in a material move as a function of time, with the aim of understanding the structural, dynamical and thermodynamical properties of complex systems. It has been successfully applied to gases, liquids, and ordered and disordered solids. In addition to equation of state, mean square displacement (MSD), velocity auto-correlation function (VACF), vibrational density of states and pair correlation function (PCF) are the most important quantities enabling us to determine various properties of interest in MD simulations.

The MSD is a measure of the deviation of the position of a particle with respect to a reference position over time. It can help to determine whether the ion is freely diffusing, transported, or bound. It is defined as

$$MSD(m) = \frac{1}{N_{\text{particles}}} \sum_{i=1}^{N_{\text{particles}}} \frac{1}{N-m} \sum_{k=0}^{N-m-1} (\mathbf{r}_i(k+m) - \mathbf{r}_i(k))^2, \quad (39)$$

where $\mathbf{r}_i(t)$ is the atom position of atom i after t time of simulation. $N_{\text{particles}}$ and N are the total number of atoms and total frames respectively. According to this definition, the MSD is averaged over all windows of length m and over all selected particles. An alternative method which can efficiently calculate MSD is proposed based on the Fast Fourier Transform (FFT) algorithm as described in Refs. [90, 91] and references therein.

If the system stays in the solid state, the MSD oscillates around a constant value. This means that all the atoms are confined to certain positions. For a liquid, however, atoms will move indefinitely and the MSD continues to increase linearly with time. This implies that sudden changes in the MSD with time are indicative of melting, solidification, phase transition, and so on. In addition, the calculation of MSD is the standard way to estimate of the parameters of movement, such as the diffusion coefficients from MD simulations. Assuming that the system is in a diffusive regime and the position measurement error is negligible, the self-diffusion coefficient D can be obtained through Einstein's relation:

$$D = \frac{1}{2Nd\Delta t} \sum_{i=1}^N \left\langle |\mathbf{r}_i(t + \Delta t) - \mathbf{r}_i(t)|^2 \right\rangle_t = \frac{MSD(\Delta t)}{2d\Delta t}, \quad (40)$$

where d is the dimensionality of the system (integer, $1 \leq d \leq 3$), N is the total number of diffusion ions, $\mathbf{r}_i(t)$ is the displacement of the i -th ion at time t and the bracket represents averaging over t . As an illustrated example, the calculated MSD and diffusion coefficient of Li^+ ions in the $\text{Li}_{10}\text{GeP}_2\text{S}_{12}$ material at 600 K is presented in Fig. 19. It is found that the diffusivity coefficient in the z direction is predicted to be one order of magnitude more than those in the x and y directions at 600 K. The calculated diffusion coefficient is $8.70 \times 10^{-5} \text{ cm}^2/\text{s}$ at 600 K, in excellent agreement with previous studies.[92]

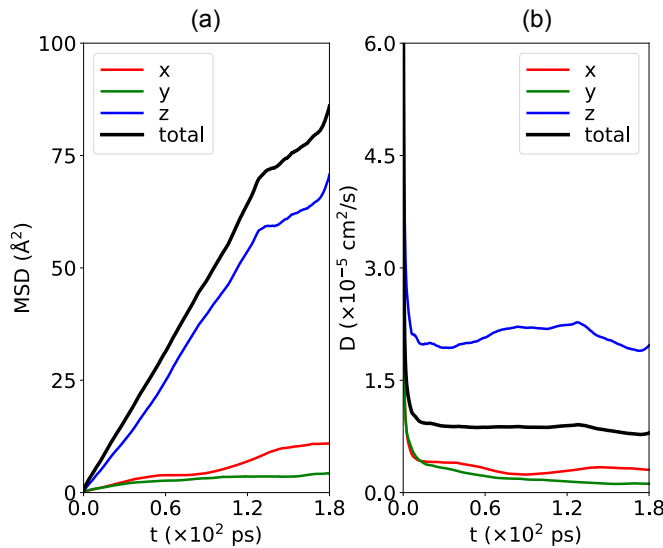


Figure 19: (Color online) Calculated the time evolution of (a) mean square displacement and (b) diffusion coefficient of Li^+ ions in the $\text{Li}_{10}\text{GeP}_2\text{S}_{12}$ at 600 K obtained from MD simulations.

The VACF is another way of checking the movement type of atoms. It is a value that basically tells until when the particle remembers its previous movements. Like for the MSD, it is a time-averaged value, defined over a delay domain. The normalized VACF is defined as

$$\gamma(t) = \frac{\sum_{i=1}^N \langle \mathbf{v}_i(t) \cdot \mathbf{v}_i(0) \rangle}{\sum_{i=1}^N \langle \mathbf{v}_i(0) \rangle^2}, \quad (41)$$

where $\mathbf{v}_i(t)$ is the velocity of the i atom at time t . The bracket denotes averages over the time origin, t_0 . The optical and thermodynamical properties of materials depend on VDOS $f(\omega)$ which can be obtained from the Fourier transform of the VACF under the harmonic approximation,[93]

$$f(\omega) = \mathcal{F}[\gamma(t)] = \int_{-\infty}^{\infty} \gamma(t) e^{-i\omega t} dt, \quad (42)$$

where ω and \mathcal{F} are the vibrational frequency and Fourier transform operator respectively.

The PCF $g(r)$ describes how atoms are distributed in a thin shell at a radius r from an arbitrary atom in the material. It is useful not only for studying the details of the system but also to obtain accurate values for the macroscopic quantities such as the potential energy and pressure. This quantity can be obtained by summing the number of atoms found at a given distance in all directions from a particular atom:

$$g(r) = \frac{dN/N}{dV/V} = \frac{1}{4\pi r^2} \frac{1}{N\rho} \sum_{i=1}^N \sum_{j \neq i}^N \langle \delta(r - |\mathbf{r}_i - \mathbf{r}_j|) \rangle, \quad (43)$$

where r is the radial distance. ρ is the average density of the entire material. The normalization via the density ensures that for large distances the radial distribution approaches unity. The partial radial distribution between two elements is calculated as

$$g_{AB}(r) = \frac{1}{4\pi r^2} \frac{N}{\rho N_A N_B} \sum_{i \in A} \sum_{j \in B, j \neq i}^N \langle \delta(r - |\mathbf{r}_i - \mathbf{r}_j|) \rangle \quad (44)$$

As an illustrated example, figure 20 shows the PBE calculated MSD, VACF, VDOS and PCF for liquid water at 400 K processed by the MD utility. Overall, our result is in good agreement with available experimental and theoretical results.[94, 95]

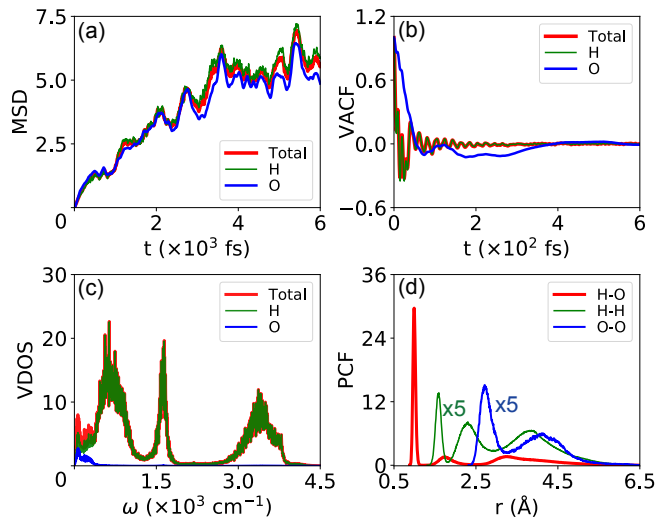


Figure 20: (Color online) Calculated (a) mean square displacement, (b) velocity autocorrelation function, (c) vibrational density of states and (d) pair correlation function of liquid water at 400 K obtained from MD simulations.

4. Conclusions

In summary, VASPKIT is a user friendly toolkit that can be easily used to perform initial setup for calculations and post-post-processing analysis to derive various material properties from the raw calculated data using VASP code. We have demonstrated its capability through providing some illustrative examples. It provides command-line interface for the purpose of performing high-throughput calculations. It remains under development, and further functionality, including closer support for other codes, is likely to be added. As the number of new features is added, we hope that VASPKIT becomes an even more attractive toolkit contributing to efficient development and utilization of electronic structure theory.

5. Acknowledgments

We acknowledge other contributors (in no particular order) including Xue-Fei Liu, Peng-Fei Liu, Zhao-Fu Zhang, Tian Wang, Dao-Xiong Wu, Ya-Chao Liu, Jiang-Shan Zhao, Qiang Li and iGo Li. We gratefully acknowledge helpful discussions with Zhe-Yong Fan, Qi-Jing Zheng and Yun-Ye Liang. We also thank various researchers around the world for reporting bugs and suggesting features, which have lead to significant improvements in the accuracy and robustness of the package. V.W. gratefully appreciates Yoshiyuki Kawazoe and Shigenobu Ogata for their invaluable support. This work was supported in part by the National Natural Science Foundational of China under (Grant No. 51877177) and the Natural Science Basic Research Plan in Shaanxi Province (Grant No. 2019JM594).

References

- [1] P. Hohenberg, W. Kohn, Inhomogeneous electron gas, *Phys. Rev.* 136 (1964) B864–B871. doi:10.1103/PhysRev.136.B864.
- [2] W. Kohn, L. J. Sham, Self-consistent equations including exchange and correlation effects, *Phys. Rev.* 140 (1965) A1133–A1138. doi:10.1103/PhysRev.140.A1133.
- [3] M. C. Payne, M. P. Teter, D. C. Allan, T. A. Arias, J. D. Joannopoulos, Iterative minimization techniques for ab initio total-energy calculations: molecular dynamics and conjugate gradients, *Rev. Mod. Phys.* 64 (1992) 1045–1097. doi:10.1103/RevModPhys.64.1045.
- [4] R. O. Jones, O. Gunnarsson, The density functional formalism, its applications and prospects, *Rev. Mod. Phys.* 61 (1989) 689–746. doi:10.1103/RevModPhys.61.689.
- [5] R. O. Jones, Density functional theory: Its origins, rise to prominence, and future, *Rev. Mod. Phys.* 87 (2015) 897–923. doi:10.1103/RevModPhys.87.897.
- [6] K. Sato, L. Bergqvist, J. Kudrnovský, P. H. Dederichs, O. Eriksson, I. Turek, B. Sanyal, G. Bouzerar, H. Katayama-Yoshida, V. A. Dinh, T. Fukushima, H. Kizaki, R. Zeller, First-principles theory of dilute magnetic semiconductors, *Rev. Mod. Phys.* 82 (2010) 1633–1690. doi:10.1103/RevModPhys.82.1633.
- [7] T. Dietl, H. Ohno, Dilute ferromagnetic semiconductors: Physics and spintronic structures, *Rev. Mod. Phys.* 86 (2014) 187–251. doi:10.1103/RevModPhys.86.187.
- [8] A. Jain, Y. Shin, K. A. Persson, Computational predictions of energy materials using density functional theory, *Nat. Rev. Mater.* 1 (1) (2016) 15004. doi:10.1038/natrevmats.2015.4.
- [9] C. Freysoldt, B. Grabowski, T. Hickel, J. Neugebauer, G. Kresse, A. Janotti, C. G. Van de Walle, First-principles calculations for point defects in solids, *Rev. Mod. Phys.* 86 (2014) 253–305. doi:10.1103/RevModPhys.86.253.
- [10] J. Pokluda, M. Černý, M. Šob, Y. Umeno, Ab initio calculations of mechanical properties: Methods and applications, *Prog. Mater. Sci.* 73 (2015) 127 – 158. doi:10.1016/j.pmatsci.2015.04.001.
- [11] L. Zhang, Y. Wang, J. Lv, Y. Ma, Materials discovery at high pressures, *Nat. Rev. Mater.* 2 (4) (2017) 17005. doi:10.1038/natrevmats.2017.5.
- [12] A. R. Oganov, C. J. Pickard, Q. Zhu, R. J. Needs, Structure prediction drives materials discovery, *Nat. Rev. Mater.* 4 (5) (2019) 331–348. doi:10.1038/s41578-019-0101-8.

- [13] X. Gonze, F. Jollet, F. A. Araujo, D. Adams, B. Amadon, T. Applencourt, C. Audouze, J.-M. Beuken, J. Bieder, A. Bokhanchuk, et al., Recent developments in the abinit software package, *Comput. Phys. Commun.* 205 (2016) 106 – 131. doi:[10.1016/j.cpc.2016.04.003](https://doi.org/10.1016/j.cpc.2016.04.003).
- [14] G. Kresse, J. Furthmüller, Efficiency of ab-initio total energy calculations for metals and semiconductors using a plane-wave basis set, *Comput. Mater. Sci.* 6 (1) (1996) 15 – 50. doi:[http://dx.doi.org/10.1016/0927-0256\(96\)00008-0](http://dx.doi.org/10.1016/0927-0256(96)00008-0).
- [15] G. Kresse, J. Furthmüller, Efficient iterative schemes for *ab initio* total-energy calculations using a plane-wave basis set, *Phys. Rev. B* 54 (1996) 11169–11186. doi:[10.1103/PhysRevB.54.11169](https://doi.org/10.1103/PhysRevB.54.11169).
- [16] J. M. Soler, E. Artacho, J. D. Gale, A. García, J. Junquera, P. Ordejón, D. Sánchez-Portal, The SIESTA method for ab initio order-n materials simulation, *J. Phys.: Condens. Matter* 14 (11) (2002) 2745–2779. doi:[10.1088/0953-8984/14/11/302](https://doi.org/10.1088/0953-8984/14/11/302).
- [17] P. Giannozzi, S. Baroni, N. Bonini, M. Calandra, R. Car, C. Cavazzoni, D. Ceresoli, G. L. Chiarotti, M. Cococcioni, I. Dabo, A. D. Corso, S. de Gironcoli, S. Fabris, G. Fratesi, R. Gebauer, U. Gerstmann, C. Gougousis, A. Kokalj, M. Lazzeri, L. Martin-Samos, N. Marzari, F. Mauri, R. Mazzarello, S. Paolini, A. Pasquarello, L. Paulatto, C. Sbraccia, S. Scandolo, G. Sclauzero, A. P. Seitsonen, A. Smogunov, P. Umari, R. M. Wentzcovitch, QUANTUM ESPRESSO: a modular and open-source software project for quantum simulations of materials, *J. Phys.: Condens. Matter* 21 (39) (2009) 395502. doi:[10.1088/0953-8984/21/39/395502](https://doi.org/10.1088/0953-8984/21/39/395502).
- [18] P. Giannozzi, O. Andreussi, T. Brumme, O. Bunau, M. B. Nardelli, M. Calandra, R. Car, C. Cavazzoni, D. Ceresoli, M. Cococcioni, et al., Advanced capabilities for materials modelling with quantum ESPRESSO, *J. Phys.: Condens. Matter* 29 (46) (2017) 465901. doi:[10.1088/1361-648x/aa8f79](https://doi.org/10.1088/1361-648x/aa8f79).
- [19] K. Dewhurst, S. Sharma, L. Nordstrom, F. Cricchio, F. Bultmark, H. Gross, C. Ambrosch-Draxl, C. Persson, C. Brouder, R. Armiento, et al., The elk fp-lapw code, ELK, <http://elk.sourceforge.net> (2016).
- [20] P. Blaha, K. Schwarz, F. Tran, R. Laskowski, G. K. H. Madsen, L. D. Marks, *Wien2k: An apw+lo program for calculating the properties of solids*, *J. Chem. Phys.* 152 (7) (2020) 074101. doi:[10.1063/1.5143061](https://doi.org/10.1063/1.5143061). URL <https://doi.org/10.1063/1.5143061>
- [21] S. P. Ong, W. D. Richards, A. Jain, G. Hautier, M. Kocher, S. Cholia, D. Gunter, V. L. Chevrier, K. A. Persson, G. Ceder, Python materials genomics (pymatgen): A robust, open-source python library for materials analysis, *Comput. Phys. Sci.* 68 (2013) 314 – 319. doi:[10.1016/j.commatsci.2012.10.028](https://doi.org/10.1016/j.commatsci.2012.10.028).
- [22] A. H. Larsen, J. J. Mortensen, J. Blomqvist, I. E. Castelli, R. Christensen, M. Dulak, J. Friis, M. N. Groves, B. Hammer, C. Hargus, et al., The atomic simulation environment—a python library for working with atoms, *J. Phys.: Condens. Matter* 29 (27) (2017) 273002. doi:[10.1088/1361-648x/aa680e](https://doi.org/10.1088/1361-648x/aa680e).
- [23] V. Wang, Y. Liang, Y. Kawazoe, W. Geng, High-throughput computational screening of two-dimensional semiconductors, arXiv preprint arXiv:1806.04285 (2018).
- [24] Y. Hinuma, G. Pizzi, Y. Kumagai, F. Oba, I. Tanaka, Band structure diagram paths based on crystallography, *Comput. Phys. Sci.* 128 (2017) 140 – 184. doi:[10.1016/j.commatsci.2016.10.015](https://doi.org/10.1016/j.commatsci.2016.10.015).
- [25] A. Togo, I. Tanaka, Spglib: a software library for crystal symmetry search, arXiv preprint arXiv:1808.01590 (2018).
- [26] A. Kokalj, Computer graphics and graphical user interfaces as tools in simulations of matter at the atomic scale, *Comput. Mater. Sci.* 28 (2) (2003) 155–168. doi:[10.1016/S0927-0256\(03\)00104-6](https://doi.org/10.1016/S0927-0256(03)00104-6).
- [27] S. R. Hall, F. H. Allen, I. D. Brown, The crystallographic information file (cif): a new standard archive file for crystallography, *Acta Crystallographica A* 47 (6) (1991) 655–685.
- [28] F. C. Bernstein, T. F. Koetzle, G. J. Williams, E. F. Meyer, M. D. Brice, J. R. Rodgers, O. Kennard, T. Shimanouchi, M. Tasumi, The protein data bank: A computer-based archival file for macromolecular structures, *J. Mol. Biol.* 112 (3) (1977) 535 – 542. doi:[10.1016/S0022-2836\(77\)80200-3](https://doi.org/10.1016/S0022-2836(77)80200-3).
- [29] K. Latimer, S. Dwaraknath, K. Mathew, D. Winston, K. A. Persson, Evaluation of thermodynamic equations of state across chemistry and structure in the materials project, *npj Comput. Mater.* 4 (1) (2018) 40. doi:[10.1038/s41524-018-0091-x](https://doi.org/10.1038/s41524-018-0091-x).

- [30] M. Hebbache, M. Zemzemi, Ab initio study of high-pressure behavior of a low compressibility metal and a hard material: Osmium and diamond, *Phys. Rev. B* 70 (2004) 224107. doi:10.1103/PhysRevB.70.224107.
- [31] P. Vinet, J. Ferrante, J. H. Rose, J. R. Smith, Compressibility of solids, *J. Geophys. Res.* 92 (B9) (1987) 9319–9325. doi:10.1029/JB092iB09p09319.
- [32] J. H. Dymond, R. Malhotra, The tait equation: 100 years on, *Int. J. Thermophys.* 9 (6) (1988) 941–951. doi:10.1007/BF01133262.
- [33] J.-P. Poirier, A. Tarantola, A logarithmic equation of state, *Phys. Earth Planet. Inter.* 109 (1) (1998) 1 – 8. doi:10.1016/S0031-9201(98)00112-5.
- [34] D. C. Pack, W. M. Evans, H. J. James, The propagation of shock waves in steel and lead, *Proc. Phys. Soc.* 60 (1) (1948) 1–8. doi:10.1088/0959-5309/60/1/302.
- [35] F. D. Murnaghan, The compressibility of media under extreme pressures, *Proc. Natl Acad. Sci* 30 (9) (1944) 244–247. doi:10.1073/pnas.30.9.244.
- [36] P. B. Roy, S. B. Roy, Applicability of isothermal three-parameter equations of state of solids—a reappraisal, *J. Phys.: Condens. Matter* 17 (39) (2005) 6193–6216. doi:10.1088/0953-8984/17/39/007.
- [37] F. Birch, Finite elastic strain of cubic crystals, *Phys. Rev.* 71 (1947) 809–824. doi:10.1103/PhysRev.71.809.
- [38] W. Voigt, et al., *Lehrbuch der kristallphysik*, Vol. 962, Teubner Leipzig, 1928.
- [39] O. H. Nielsen, R. M. Martin, First-principles calculation of stress, *Phys. Rev. Lett.* 50 (1983) 697–700. doi:10.1103/PhysRevLett.50.697.
- [40] O. Nielsen, R. M. Martin, Stresses in semiconductors: Ab initio calculations on si, ge, and gaas, *Physical Review B* 32 (6) (1985) 3792. doi:10.1103/PhysRevB.32.3792.
- [41] S. Zhang, R. Zhang, Aelas: Automatic elastic property derivations via high-throughput first-principles computation, *Comput. Phys. Commun.* 220 (2017) 403 – 416. doi:10.1016/j.cpc.2017.07.020.
- [42] R. Golesorkhtabar, P. Pavone, J. Spitaler, P. Puschnig, C. Draxl, Elastic: A tool for calculating second-order elastic constants from first principles, *Comput. Phys. Commun.* 184 (8) (2013) 1861 – 1873. doi:10.1016/j.cpc.2013.03.010.
- [43] J. F. Nye, et al., *Physical properties of crystals: their representation by tensors and matrices*, Oxford university press, 1985.
- [44] Y. Le Page, P. Saxe, Symmetry-general least-squares extraction of elastic coefficients from ab initio total energy calculations, *Physical Review B* 63 (17) (2001) 174103. doi:10.1103/PhysRevB.63.174103.
- [45] R. Yu, J. Zhu, H. Ye, Calculations of single-crystal elastic constants made simple, *Comput. Phys. Commun.* 181 (3) (2010) 671 – 675. doi:10.1016/j.cpc.2009.11.017.
- [46] Y. Le Page, P. Saxe, Symmetry-general least-squares extraction of elastic data for strained materials from ab initio calculations of stress, *Phys. Rev. B* 65 (2002) 104104. doi:10.1103/PhysRevB.65.104104.
- [47] Z. Hashin, S. Shtrikman, A variational approach to the theory of the elastic behaviour of polycrystals, *J. Mech. Phys. Solids* 10 (4) (1962) 343 – 352. doi:10.1016/0022-5096(62)90005-4.
- [48] F. Mouhat, F. m. c.-X. Coudert, Necessary and sufficient elastic stability conditions in various crystal systems, *Phys. Rev. B* 90 (2014) 224104. doi:10.1103/PhysRevB.90.224104.
- [49] A. Reuss, Z. Angnew, A calculation of the bulk modulus of polycrystalline materials, *Math Meth* 9 (1929) 55. doi:10.1007/BF00544497.
- [50] R. Hill, The elastic behaviour of a crystalline aggregate, *Proc. Phys. Soc. London, Sect. A* 65 (5) (1952) 349–354. doi:10.1088/0370-1298/65/5/307.
- [51] M. Maździarz, Comment on ‘the computational 2d materials database: high-throughput modeling and discovery of atomically thin crystals’, *2D Mater.* 6 (4) (2019) 048001. doi:10.1088/2053-1583/ab2ef3.

- [52] L. D. Landau, E. M. Lifshitz, Course of Theoretical Physics Vol 7: Theory and Elasticity, Pergamon press, 1959.
- [53] X. Wei, B. Fragneaud, C. A. Marianetti, J. W. Kysar, Nonlinear elastic behavior of graphene: Ab initio calculations to continuum description, Phys. Rev. B 80 (2009) 205407. doi:10.1103/PhysRevB.80.205407.
- [54] S. Haastrup, M. Strange, M. Pandey, T. Deilmann, P. S. Schmidt, N. F. Hinsche, M. N. Gjerding, D. Torelli, P. M. Larsen, A. C. Riis-Jensen, et al., The computational 2d materials database: high-throughput modeling and discovery of atomically thin crystals, 2D Mater. 5 (4) (2018) 042002. doi:10.1088/2053-1583/aacfc1.
- [55] L. Wang, A. Kutana, X. Zou, B. I. Yakobson, Electro-mechanical anisotropy of phosphorene, Nanoscale 7 (2015) 9746–9751. doi:10.1039/C5NR00355E.
- [56] V. Wang, Y. Liang, Y. Kawazoe, W. Geng, High-throughput computational screening of two-dimensional semiconductors, arXiv preprint arXiv:1806.04285 (2018).
- [57] J. D. Hunter, Matplotlib: A 2d graphics environment, Comput. Sci. Eng. 9 (3) (2007) 90–95. doi:10.1109/MCSE.2007.55.
- [58] L. D. Whalley, J. M. Frost, B. J. Morgan, A. Walsh, Impact of nonparabolic electronic band structure on the optical and transport properties of photovoltaic materials, Phys. Rev. B 99 (2019) 085207. doi:10.1103/PhysRevB.99.085207.
- [59] A. J. Williamson, L. W. Wang, A. Zunger, Theoretical interpretation of the experimental electronic structure of lens-shaped self-assembled InAs/GaAs quantum dots, Phys. Rev. B 62 (2000) 12963–12977. doi:10.1103/PhysRevB.62.12963.
- [60] H. Morkoç, Ü. Özgür, Zinc oxide: fundamentals, materials and device technology, John Wiley & Sons, 2008.
- [61] N. Naka, K. Fukai, Y. Handa, I. Akimoto, Direct measurement via cyclotron resonance of the carrier effective masses in pristine diamond, Phys. Rev. B 88 (2013) 035205. doi:10.1103/PhysRevB.88.035205.
- [62] K. Momma, F. Izumi, VESTA3 for three-dimensional visualization of crystal, volumetric and morphology data, J. Appl. Crystallogr. 44 (6) (2011) 1272–1276. doi:10.1107/S0021889811038970.
- [63] M. Frisch, G. Trucks, H. B. Schlegel, G. Scuseria, M. Robb, J. Cheeseman, G. Scalmani, V. Barone, B. Mennucci, G. Petersson, et al., Gaussian 09, revision a. 02, gaussian, Inc., Wallingford, CT 200 (2009) 28.
- [64] M. Peressi, N. Binggeli, A. Baldereschi, Band engineering at interfaces: theory and numerical experiments, J. Phys. D: Appl. Phys. 31 (11) (1998) 1273–1299. doi:10.1088/0022-3727/31/11/002.
- [65] A. Kahn, Fermi level, work function and vacuum level, Mater. Horiz. 3 (1) (2016) 7–10. doi:10.1039/C5MH00160A.
- [66] V. Popescu, A. Zunger, Effective band structure of random alloys, Phys. Rev. Lett. 104 (2010) 236403. doi:10.1103/PhysRevLett.104.236403.
- [67] V. Popescu, A. Zunger, Extracting e versus k effective band structure from supercell calculations on alloys and impurities, Phys. Rev. B 85 (2012) 085201. doi:10.1103/PhysRevB.85.085201.
- [68] M. Gajdoš, K. Hummer, G. Kresse, J. Furthmüller, F. Bechstedt, Linear optical properties in the projector-augmented wave methodology, Phys. Rev. B 73 (2006) 045112. doi:10.1103/PhysRevB.73.045112.
- [69] M. Fox, Optical properties of solids (2002).
- [70] L. Hedin, New method for calculating the one-particle green's function with application to the electron-gas problem, Phys. Rev. 139 (3A) (1965) A796. doi:10.1103/PhysRev.139.A796.
- [71] F. Fuchs, J. Furthmüller, F. Bechstedt, M. Shishkin, G. Kresse, Quasiparticle band structure based on a generalized kohn-sham scheme, Phys. Rev. B 76 (11) (2007) 115109. doi:10.1103/PhysRevB.76.115109.
- [72] G. Onida, L. Reining, A. Rubio, Electronic excitations: density-functional versus many-body green's-function approaches, Rev. Mod. Phys. 74 (2002) 601–659. doi:10.1103/RevModPhys.74.601.

- [73] F. Hüser, T. Olsen, K. S. Thygesen, How dielectric screening in two-dimensional crystals affects the convergence of excited-state calculations: Monolayer mos_2 , *Phys. Rev. B* 88 (2013) 245309. doi:10.1103/PhysRevB.88.245309.
- [74] P. Cudazzo, I. V. Tokatly, A. Rubio, Dielectric screening in two-dimensional insulators: Implications for excitonic and impurity states in graphane, *Phys. Rev. B* 84 (2011) 085406. doi:10.1103/PhysRevB.84.085406.
- [75] L. Matthes, O. Pulci, F. Bechstedt, Optical properties of two-dimensional honeycomb crystals graphene, silicene, germanene, and tinene from first principles, *New J. Phys.* 16 (10) (2014) 105007. doi:10.1088/1367-2630/16/10/105007.
- [76] L. Matthes, O. Pulci, F. Bechstedt, Influence of out-of-plane response on optical properties of two-dimensional materials: First principles approach, *Phys. Rev. B* 94 (2016) 205408. doi:10.1103/PhysRevB.94.205408.
- [77] Z. Torbatian, R. Asgari, Optical absorption properties of few-layer phosphorene, *Phys. Rev. B* 98 (2018) 205407. doi:10.1103/PhysRevB.98.205407.
- [78] M. S. Dresselhaus, *Solid state physics part ii optical properties of solids* (2001).
- [79] W.-J. Yin, T. Shi, Y. Yan, Unique properties of halide perovskites as possible origins of the superior solar cell performance, *Adv. Mater.* 26 (27) (2014) 4653–4658. doi:10.1002/adma.201306281.
- [80] Transition dipole moment, https://en.wikipedia.org/w/index.php?title=Transition_dipole_moment&oldid=902785194/, accessed October 4, 2019.
- [81] W. Meng, X. Wang, Z. Xiao, J. Wang, D. B. Mitzi, Y. Yan, Parity-forbidden transitions and their impact on the optical absorption properties of lead-free metal halide perovskites and double perovskites, *J. Phys. Chem. Lett.* 8 (13) (2017) 2999–3007. doi:10.1021/acs.jpcllett.7b01042.
- [82] M. Kawamura, Fermisurfer: Fermi-surface viewer providing multiple representation schemes, *Comput. Phys. Commun.* 239 (2019) 197–203. doi:10.1016/j.cpc.2019.01.017.
- [83] S. B. Dugdale, Life on the edge: a beginner’s guide to the fermi surface, *Phys. Scr.* 91 (5) (2016) 053009. doi:10.1088/0031-8949/91/5/053009.
- [84] J. K. Nørskov, F. Studt, F. Abild-Pedersen, T. Bligaard, *Fundamental Concepts in Heterogeneous Catalysis*, 1st Edition, Wiley, 2014.
- [85] B. Hammer, J. Nørskov, Electronic factors determining the reactivity of metal surfaces, *Surf. Sci.* 343 (3) (1995) 211 – 220. doi:10.1016/0039-6028(96)80007-0.
- [86] B. Hammer, J. Nørskov, Theoretical surface science and catalysis?calculations and concepts, in: *Impact of Surface Science on Catalysis*, Vol. 45 of *Advances in Catalysis*, Academic Press, 2000, pp. 71 – 129. doi:10.1016/S0360-0564(02)45013-4.
- [87] D. A. McQuarrie, J. D. Simon, *Molecular thermodynamics*, 1999.
- [88] J. W. Ochterski, *Thermochemistry in gaussian*, Gaussian Inc (2000) 1–19.
- [89] M. Chase, *Tables, nist-janaf thermochemical*, *J. Phys. Chem. Ref. Data Monograph* 9 (1998) 12.
- [90] G. R. Kneller, V. Keiner, M. Kneller, M. Schiller, nmoldyn: A program package for a neutron scattering oriented analysis of molecular dynamics simulations, *Computer Physics Communications* 91 (1) (1995) 191–214. doi:10.1016/0010-4655(95)00048-K.
- [91] T. Róg, K. Murzyn, K. Hinsen, G. R. Kneller, nmoldyn: A program package for a neutron scattering oriented analysis of molecular dynamics simulations, *J. Comput. Chem.* 24 (5) (2003) 657–667. doi:10.1002/jcc.10243.
- [92] Y. Mo, S. P. Ong, G. Ceder, First principles study of the $\text{li}_{10}\text{gep}_{2\text{s}12}$ lithium super ionic conductor material, *Chem. Mater.* 24 (1) (2012) 15–17. doi:10.1021/cm203303y.
- [93] J. M. DICKEY, A. PASKIN, Computer simulation of the lattice dynamics of solids, *Phys. Rev.* 188 (1969) 1407–1418. doi:10.1103/PhysRev.188.1407.

- [94] A. K. Soper, C. J. Benmore, Quantum differences between heavy and light water, *Phys. Rev. Lett.* 101 (2008) 065502. doi:[10.1103/PhysRevLett.101.065502](https://doi.org/10.1103/PhysRevLett.101.065502).
- [95] S. Imoto, S. S. Xantheas, S. Saito, Molecular origin of the difference in the hoh bend of the ir spectra between liquid water and ice, *J. Chem. Phys.* 138 (5) (2013) 054506. doi:[10.1063/1.4789951](https://doi.org/10.1063/1.4789951).